

The Use of Energy Correlation functions to investigate $H \rightarrow b\bar{b}$ in Monte Carlo

Nicole Hartman

Mentor: Prof Stephen Sekula

Southern Methodist University, Dallas, Texas 75275-0175 USA

E-mail: nhartman@smu.edu

ABSTRACT:

The abstract abstract. Fill in last.

Contents

1	Introduction	3
1.1	Electroweak Symmetry Breaking	3
1.2	Large Hadron Collider	4
2	ATLAS Detector	5
2.1	ATLAS Coordinate System	5
2.2	Data Acquisition Triggers	6
2.3	Inner Detector	6
2.3.1	Pixel Tracking System	7
2.3.2	Silicon Microstrip Trackers	11
2.3.3	Transition Radiation Tracker	12
2.4	ECAL	13
2.4.1	Sampling vs. Homogenous Calorimeters	13
2.4.2	Liquid Argon Detector	14
2.4.3	GEANT 4 Simulations	14
2.5	HCAL	23
2.5.1	Tile Calorimeter	23
2.5.2	LAr hadronic end-cap calorimeter	23
2.5.3	LAr forward calorimeter	24
2.6	Muon Spectrometer	24
2.6.1	Toroidal Magnets	24
2.6.2	Monitored Drift Tubes	24
2.6.3	Cathode Strip Chambers	25
2.6.4	Level I Muon Trigger	25
2.7	Forward Detectors	26
3	Higgs Decay Modes	27
4	Jets	29
4.1	b tagging	29
5	Energy Correlation Functions	30
5.1	C1 Discriminating Variable	32
5.2	C2 Discriminating Variable	32
5.3	Applications to this analysis	32
6	Results	33
6.1	C1 Discriminating Variable	33
6.2	C2 Discriminating Variable	33
6.2.1	Likelihood function cuts	33
6.2.2	Optimization of Bc2	33

7	Future Work	33
8	Acknowledgements	33

List of Figures

1	Particles in the Standard Model [2]	3
2	Scalar Potential for $\mu^2 < 0$, called the “Mexican hat potential” [8]	4
3	Cut away of the ATLAS detector [12]	5
4	“The ATLAS Inner Detector ” [14]	6
5	“Parameters for the inner detector ” [12]	7
6	“Structural elements for ID at $\eta = 0.3.$ ” [12]	8
7	‘Structural elements for ID at $\eta = 1.4.$ ” [12]	8
8	Schematic for the general idea for how a pixel detector tracks incident particles. [16]	9
9	“Comparison of depletion zones in n ⁺ -in-n pixel sensors before (a) and after (b) type inversion. Before type inversion, the electrical field grows from the backside and reaches the pixel implants (full depletion). After type inversion the depletion zone grows from the pixel side and allows operation even if the bulk is not fully depleted.” [14]	10
10	“(Evolution of effective charge densities and full depletion voltage in standard oxygenated silicon during irradiation with various hadrons. In oxygenated silicon the increase after type inversion induced by charged particles (pions, protons) is significantly lower.” [14]	11
11	“A schematic view of the active region of the pixel detector consisting of barrel and endcap layers” [14]	11
12	Principle of operation for the TRT [21]	12
13	Schematic illustrating how a <i>sampling calorimeter</i> causes an incident particle to form a shower more quickly. [32]	13
14	Accordian sampling structure for calorimeter. [24]	14
15	Wedge showing the accordian structure for the liquid Argon portion of the calorimeter. [24]	15
16	Detector simulation for a GEANT 4 simulation. [23]	16
18	Pair production skewed by Lorentz force.	16
17	ID radiation lengths. [23]	17
19	Table for the number of cells used for clustering. [23]	17
20	Simulation demonstrating how including a presampler allows better energy reconstruction [23].	18
21	Reconstruction of the energy in the ECAL [23].	19
22	Reconstruction of the energy in the ECAL [23].	20
23	Reconstruction of the energy in the ECAL [23].	21

24	$H \rightarrow \gamma\gamma$ [23].	21
25	Reconstruction of invariant mass for a 130 GeV Higgs with $H \rightarrow 4 e-$ decay mode [23].	22
26	Calorimeter system at ATLAS [12].	23
27	Main parameters for the Muon Spectrometer. The values in parentheses refer to the configuration from 2009 [12].	25
28	Monitored Drift Tubes: MDTs	26
29	Muon trigger [22].	27
30	ATLAS figures for the channels used for the 2012 Higgs boson discovery	28
31	Cross [3]	28
32	ATLAS figures for the channels used for the 2012 Higgs boson discovery	29
33	“A secondary vertex with a significant decay length indicates the presence of a long-lived particle in the jet” [35]	30

1 Introduction

On July 4th, 2012, the ATLAS and CMS experiments jointly announced their discovery of the Higgs boson [1], culminating the experimental verification of the particles hypothesized by the Standard Model (SM)[2]. After the Higgs has been discovered, the scientific community is interested in studying its properties, for example, investigating the Higgs self-coupling by looking for di-Higgs decays. The most common decay mode for the Higgs is to b quarks [3], but this channel can be difficult to distinguish from QCD background.

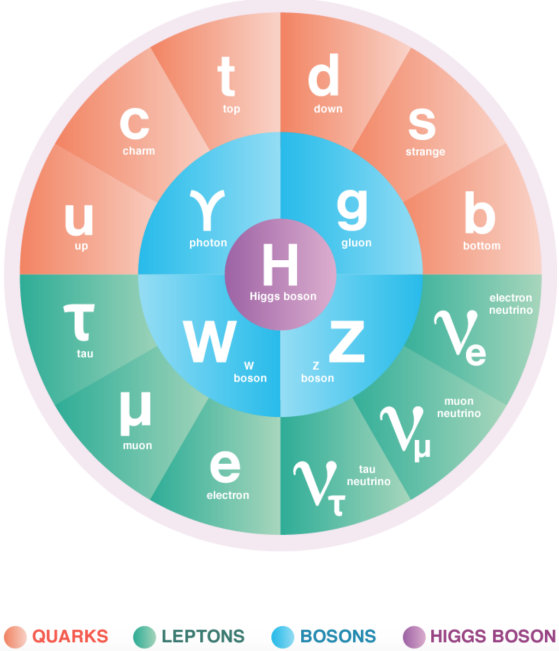


Figure 1: Particles in the Standard Model [2]

1.1 Electroweak Symmetry Breaking

The Higgs particle was originally formulated to provide masses for the W and Z bosons, the carriers for the weak force. Electroweak theory provided the unification of the electromagnetic and weak forces, and culminated with the formulation of the SM, which successfully categorized the fundamental particles and their interactions. However, as originally formulated, the SM predicated massless force carriers. The photon was known to be massless, but experiment had already concluded that the W and Z were massive. This discrepancy was solved in the 1960s, Peter Higgs and François Englert proposed spontaneous symmetry breaking to explain the discrepancy [4–8]. In Fig. 2, the scalar potential field they proposed is shown. The potential is even and symmetric about the origin, but the origin does not correspond to a local minimum. They proposed nature starts in the symmetric point, but random fluctuations causes a drop into a local minimum.

Therefore, what we observe today in nature does not look symmetric, but the symmetry of nature is replaced with a symmetry of possible solutions. As a consequence of this theory,

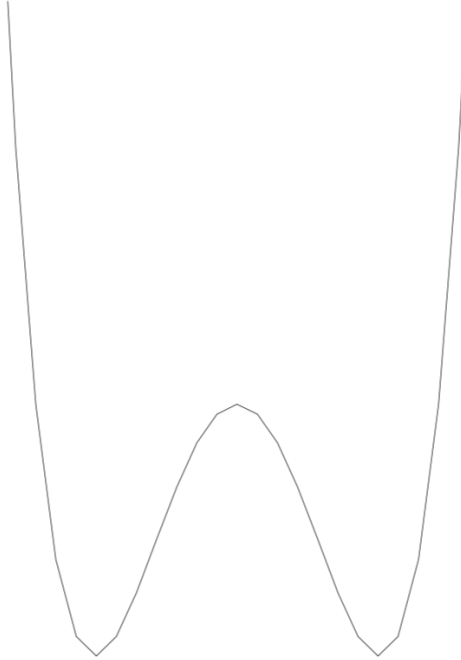


Figure 2: Scalar Potential for $\mu^2 < 0$, called the “Mexican hat potential” [8]

three of the four of the original fields are “eaten-up” by the W^\pm and Z bosons, and the remaining field is the Higgs field. As a consequence, the leptons also gain mass, as particles that interact more strongly with the Higgs field gain more mass. However, this does not lessen the number of inputs to the SM as the inputs of the particles’ masses are replaced by inputs replaced with inputs of the particles’ couplings to the Higgs field.

Since every field has an associated particle [9], the Large Hadron Collider (LHC) in Europe was built to probe the high energy regime to search for Higgs, particle, the visible manifestation of the Higgs field. Since the Higgs discovery announcement, the 2013 Nobel Prize for physics was awarded to Peter Higgs and François Englert for their formulation of the theory of supersymmetry breaking [10].

1.2 Large Hadron Collider

The Large Hadron Collider (LHC) is a 27 km particle accelerator straddling the border between France and Switzerland [11]. It collides bunches of 10^9 protons every 25 ns at a center of mass energy of 13 TeV [12]. Bunches of protons are used because since the proton radius is \sim fm, the probability of a head on collision can be increased by increasing the number of colliding particles.

Since the proton is not an elementary particle, even a head on collision will not have all of the available energy concentrated at a point. The proton is a composite particle made up of two up and one down valence quarks, along with a sea of virtual particles that spontaneously come out of the vacuum because of the uncertainty relation $\Delta E \Delta t \geq \frac{\hbar}{2}$. The 6.5 TeV per proton is distributed among the proton’s constituents. Therefore, to look

at the high energy regime, we are interested in a hard scatter where a single quark or gluon carrying a large fraction of one of the proton's momentum collides with a high energy constituent of the other proton.

Because the Higgs has a short lifetime of 10^{-22} s [13], the Higgs itself is not detected, but rather its decay products which are absorbed in the detectors at collision sites around the LHC ring. The two general purpose detectors at the LHC are ATLAS (A Toroidal LHC ApparatuS) and CMS (Compact Muon Solenoid). SMU is affiliated with the ATLAS experiment, and the MC samples used in this study were from the ATLAS collaboration, so it is useful to investigate the design of the ATLAS detector.

2 ATLAS Detector

In Fig. 3 there is a cutaway view of the ATLAS detector. The inner detector shows the tracking information leading out of the interaction point. The inner detector is immersed in a solenoid with a 2 T field to produce the curvature to allow a momentum measurement. Then the energy measurement is made in two parts, within an electromagnetic and hadronic

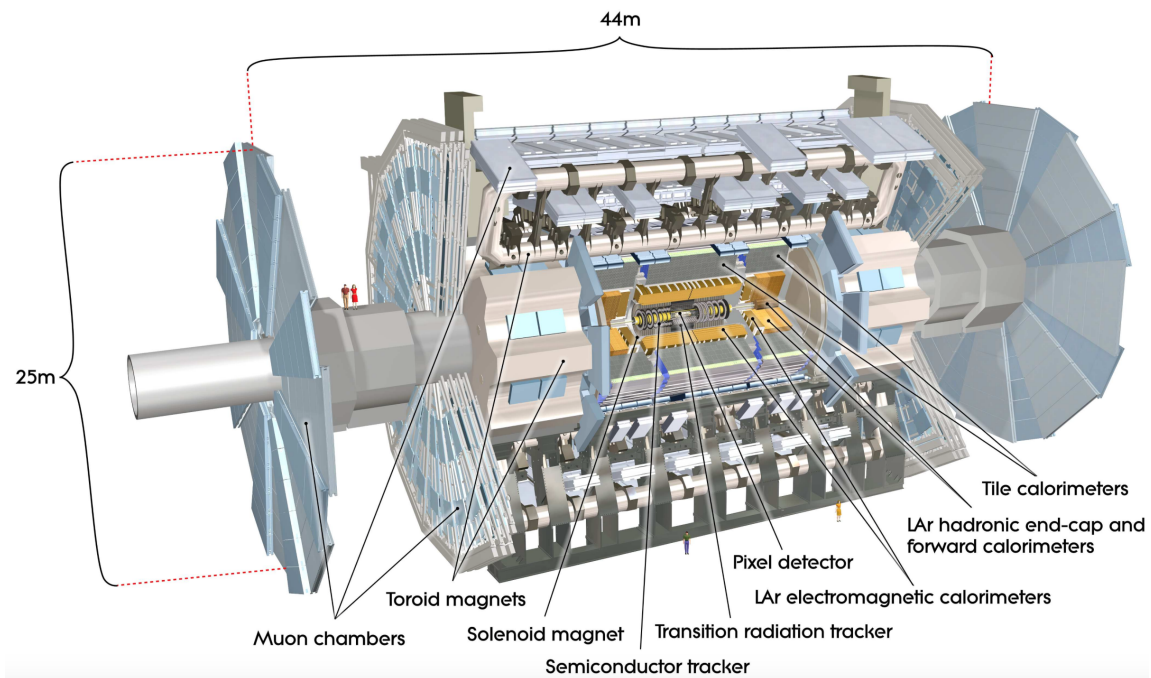


Figure 3: Cut away of the ATLAS detector [12]

calorimeters. Finally, the outermost layer of the detector is for the muon spectrometer, with a 4 T field provided by a collection of toroids.

2.1 ATLAS Coordinate System

The cylindrical coordinate system is used for the ATLAS detector, where the z-axis is measured along the beam pipe, the x-axis points into the center of the ring, and y-axis points

vertically up. Normally, we use $\phi = \arctan(\frac{y}{x})$ the azimuthal angle, to denote orientation in the plane transverse to the beam, and use the pseudorapidity η , the pseudorapidity, as a measure of the polar angle inside the detector, where

$$\eta = -\ln(\tan(\frac{\theta}{2})) \quad (2.1)$$

where $\theta \in [0, \pi]$ is the polar angle as measured from the z-axis. The ATLAS detector is forward-backward symmetric to maximize the detector coverage since colliding protons each have the same energy.

2.2 Data Acquisition Triggers

At ATLAS, with the high fluency of particles there is no way that all of the events can be recorded. There are three stages of triggers that discriminate which events should be written to memory. The Level I trigger is implemented in hardware before the information from an event even gets sent to a computing farm, and these Level I Triggering electronics need to be fast and efficient enough to pass on a manageable work load to the Level II triggering system [12].

2.3 Inner Detector

In Fig. 4, a cutaway view of the inner detector (ID) for ATLAS is shown. With approx-

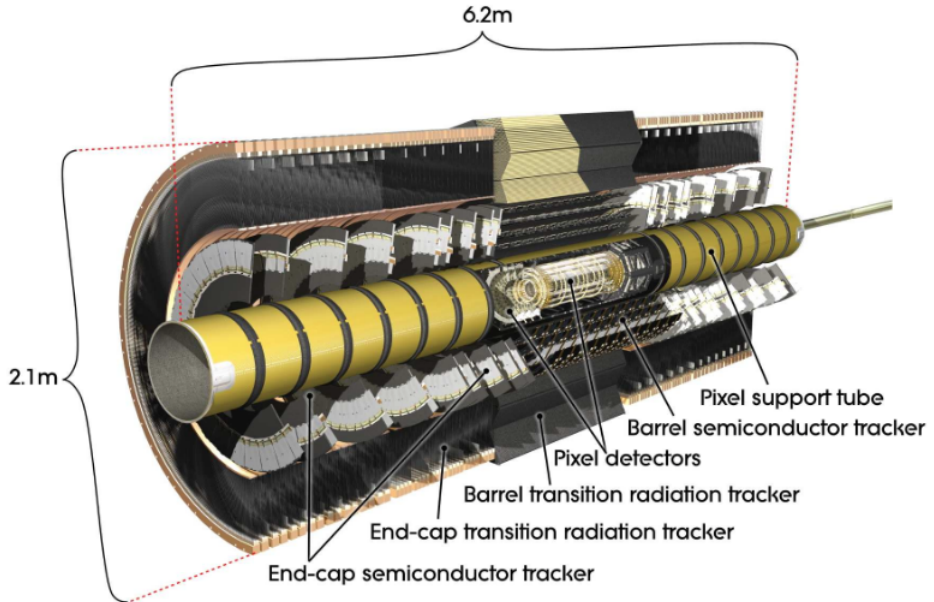


Figure 4: “The ATLAS Inner Detector ” [14]

imately 1000 tracks emerging from the interaction point every 25 ns, the ID is divided into 3 different regions to optimize the pattern recognition and momentum measurement algorithms [12]. The pixel detectors have the most accuracy, so this layer is placed closest to the interaction point. The pixel detector also has the highest cost, so the next least

Item		Radial extension (mm)	Length (mm)
Overall ID envelope		$0 < R < 1150$	$0 < z < 3512$
Beam-pipe		$29 < R < 36$	
Pixel	Overall envelope	$45.5 < R < 242$	$0 < z < 3092$
3 cylindrical layers	Sensitive barrel	$50.5 < R < 122.5$	$0 < z < 400.5$
2×3 disks	Sensitive end-cap	$88.8 < R < 149.6$	$495 < z < 650$
SCT	Overall envelope	$255 < R < 549$ (barrel) $251 < R < 610$ (end-cap)	$0 < z < 805$ $810 < z < 2797$
4 cylindrical layers	Sensitive barrel	$299 < R < 514$	$0 < z < 749$
2×9 disks	Sensitive end-cap	$275 < R < 560$	$839 < z < 2735$
TRT	Overall envelope	$554 < R < 1082$ (barrel) $617 < R < 1106$ (end-cap)	$0 < z < 780$ $827 < z < 2744$
73 straw planes	Sensitive barrel	$563 < R < 1066$	$0 < z < 712$
160 straw planes	Sensitive end-cap	$644 < R < 1004$	$848 < z < 2710$

Figure 5: “Parameters for the inner detector ” [12]

expensive tracking option is the silicon microstrip trackers (SCTs), at the next farthest region away from the interaction point. Finally, the Transition Radiation Trackers (TRTs) compose the outermost region of the inner detector. The ID uses pattern recognition to measure transverse momentum as low as 0.5 GeV, and provides electron identification for $|\eta| < 2.0$ for energies up to 150 GeV [12]. Displaced vertexes provided by the pixel detector also can identify short lived particles decaying to B-mesons.

2.3.1 Pixel Tracking System

The general purpose ATLAS detector at the Large Hadron Collider (LHC) is often referred to as a “giant camera” [18]. In a general sense, both a camera and the ATLAS detector provide ways to remember special events, but the parallels run deeper than their purposes, since both cameras and particle detectors can garner information via pixels. In a camera, an incident photon will go through a Silicon diode and knock a valence electron free to generate a few electron hole pairs. An electric field is set up across the pixel and will then pull the electron and hole apart to the metal contacts where the charge can be read out. A pixel detector at ATLAS works in a similar way, except the energy of the incident particles that at ATLAS is orders of magnitude larger: while an photon of visible light has an energy of a few eV, typical “interesting” particles at the LHC are in the keV to MeV range.

The pixel detectors do not “absorb” particles, but rather, as a particle passes through the pixel sensor, it creates a train of freed electrons and these electron hole pairs which are separated by the electric field read out the information by the electronics, as shown in Fig. 8.

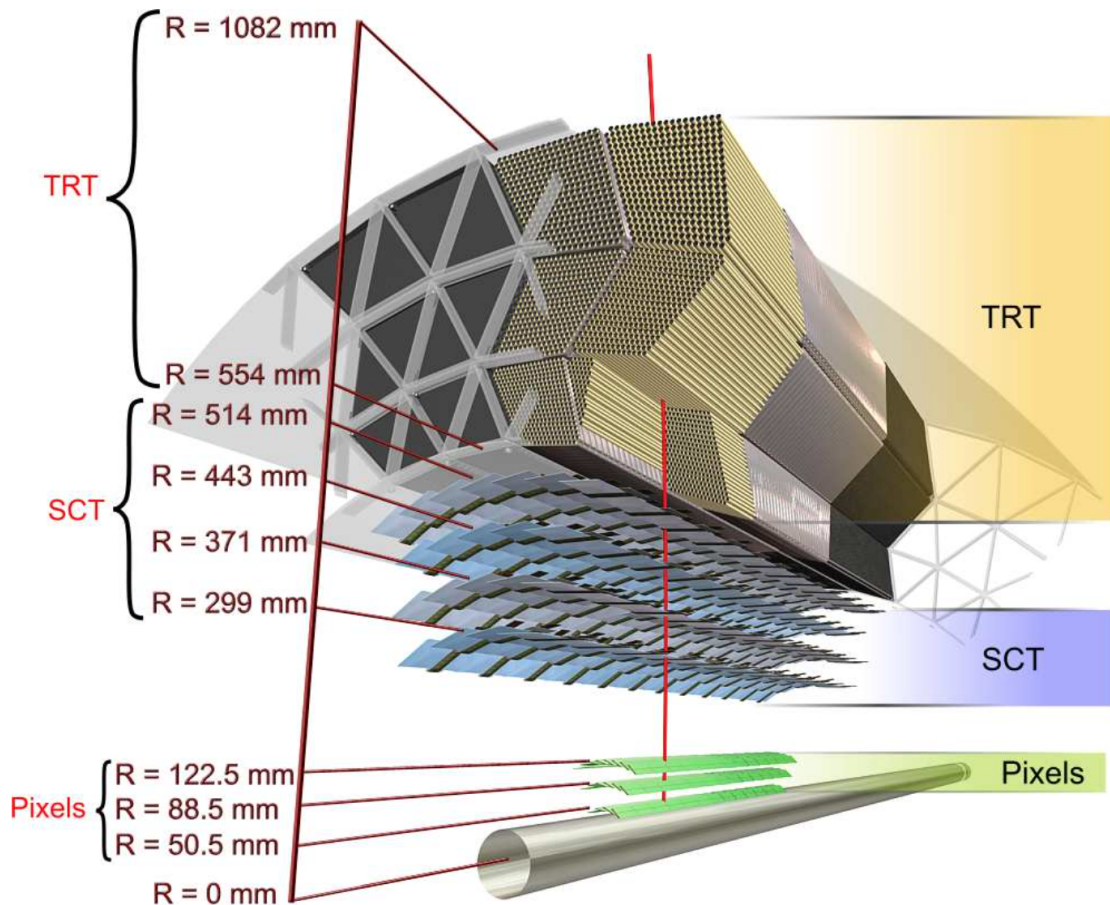


Figure 6: “Structural elements for ID at $\eta = 0.3.$ ” [12]

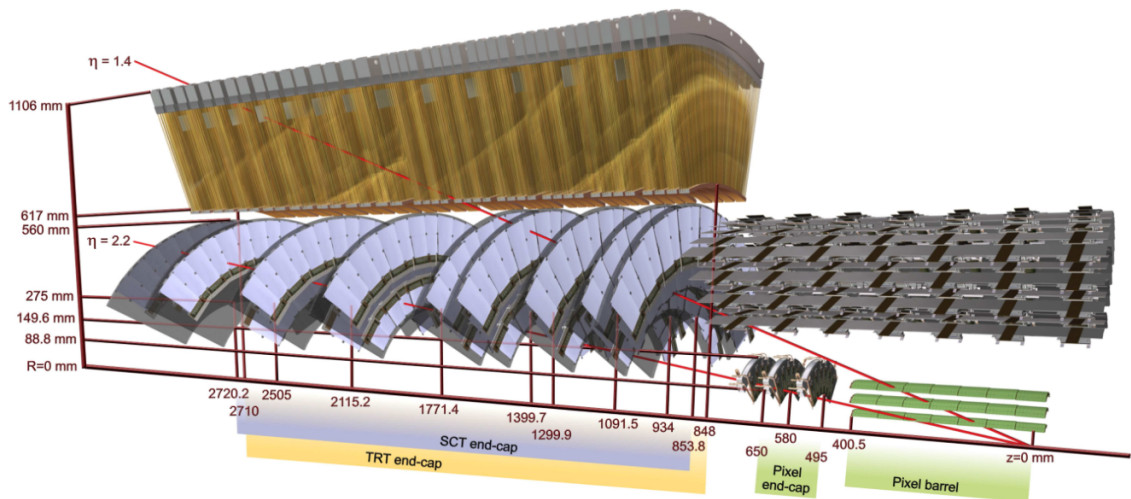


Figure 7: ‘Structural elements for ID at $\eta = 1.4.$ ” [12]

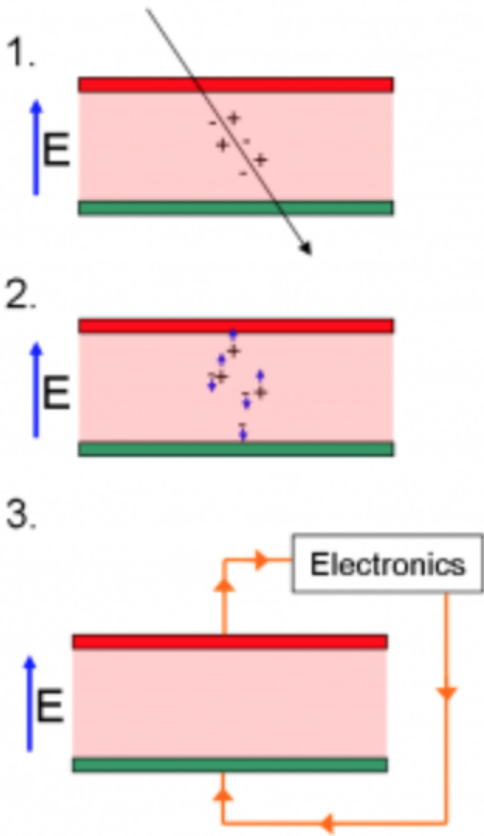


Figure 8: Schematic for the general idea for how a pixel detector tracks incident particles. [16]

the electron infused intrinsic region. These regions of positive and negative charge will create a built-in electric field which will oppose the diffusion of the electrons away from the n⁺-region. Finally, on the other end of the pixel region you can create another n-type contact region, and to prevent the flow of electrons away from this n-type region to create an n⁺-in-n, a voltage difference is applied across the two contacts as shown in Fig. 9. Grounding the n bulk while providing an negative voltage at the n⁺ contact creates an electric field pointing from the ground to negative bias voltage which provides a potential barrier to keep the electron in the n-region.

When an incident particle crosses through the intrinsic region of the detector and generates electron hole pairs, the holes will be drawn to the lower voltage while the electrons will be drawn to the grounded n-region to be read out by the electronics. However, with all of the holes drawn to the n-region, the surplus of holes will eventually balance become greater than the number of electrons, and the n⁺-region will turn into a p-type region, as shown in Fig. 9. Now since the pixel sensor has both a p and an n type region, it constitutes a diode, and since we have a negative voltage is applied to the p-side, this diode is operating in reverse bias.

The pixel sensors at ATLAS consist of 80 million [17] rectangular $50\mu\text{m} \times 400\mu\text{m}$ n⁺-in-n electrodes. The n⁺-in-n refers to the regions of the sensor, n⁺ is an electron rich region, where the positive charge comes from the diffusion of electrons away from the region. This n region is created by infusing the bulk silicon (which has 4 valence electrons) with nitrogen atoms (which have five valence electrons). When these dopant atoms bond interstitially with the silicon atoms, four of nitrogen's electrons will form covalent bonds with the surrounding silicon atoms, but one of the electrons will be left partnerless. The second law of thermodynamics states that systems tend to states of greater randomness, therefore the higher concentration of electrons in the n-doped region will want to *diffuse* into the undoped, or *intrinsic* region of the silicon bulk. The dopant atoms that were diffused to create the n-type region were originally neutral with equal numbers of protons and neutrons, but as the electrons leave the doped region the nitrogen atoms gives the n-type region a positive electric charge while a negative charge will extend into some layer of

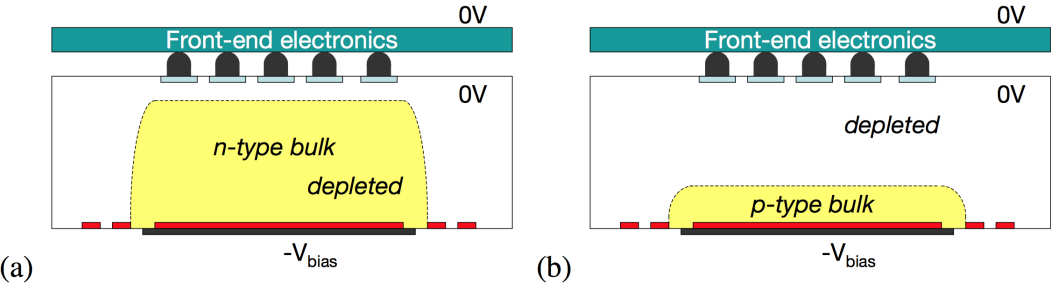


Figure 9: “Comparison of depletion zones in n^+ -in- n pixel sensors before (a) and after (b) type inversion. Before type inversion, the electrical field grows from the backside and reaches the pixel implants (full depletion). After type inversion the depletion zone grows from the pixel side and allows operation even if the bulk is not fully depleted.” [14]

Figure 10 shows how the effective density of charge carriers varies as a function of the incident particle inverse cross-section. The cusp of the V-shaped curve shows where the type inversion occurs because at first when the holes go to the negative potential n^+ region this decreases the available charge carriers per unit volume, but then after the type inversion, the number of incident charge carriers will make the region increasingly more p-type. The figure shows that, in pure silicon, rate at which the effective charge carrier density grows as a function of the incident flux is much faster than the rate at which the negative charge carriers decreased. This is a problem, because if there are too many charge carriers, this p-type region can grow large enough so that a conductive channel forms between the two contacts, and the sensor will not be able to separate the electrons and holes to detect incident particles anymore. This rate of charge carrier increase can be moderated by using oxygen infused silicon. Oxygen acts like an insulator, and therefore will tend to fight the tendency to create electron-hole pairs to create a sensor that will be able to last longer.

Figure 4 shows how the pixel detector fits in with the rest of the components of the inner detector. Zooming in on Fig. 4, Fig. 11 shows the innermost part of the inner detector: the pixel detector. It consists of 80 million channels divided into 4 cylindrical layers combined in a volume 1442 mm in length with 430 mm radius [14].

Since the pixel detector seeks to gain as much information about the central reaction as possible, the pixel detector needs to be as close to the beam pipe as possible. Therefore, the pixel detector starts just 5 cm from the center of the beam pipe and has coverage for $|\eta| < 2.5$ [17]. Since the pixel detector is so close to the interaction point, its electronics must be able to withstand high radiation doses of up to 500-kGy. The pn diodes can experience a leakage current when an electron hole pair has enough energy to overcome the potential barrier. To minimize this leakage current the detector was designed to minimize the number of electron hole pairs spontaneously generated by cooling the system at -6°C . The pixel detector has a resolution of 15 microns with rectangular pixels of $50\mu\text{m} \times 400\mu\text{m}$, and this precision is limited by the size of the electronics.

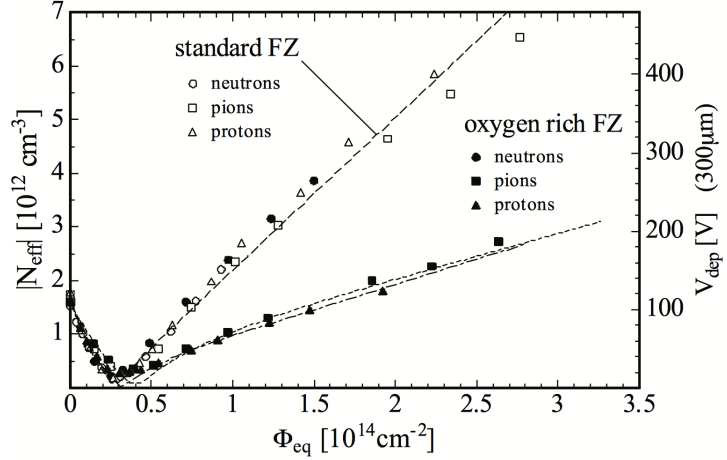


Figure 10: “(Evolution of effective charge densities and full depletion voltage in standard oxygenated silicon during irradiation with various hadrons. In oxygenated silicon the increase after type inversion induced by charged particles (pions, protons) is significantly lower.” [14]

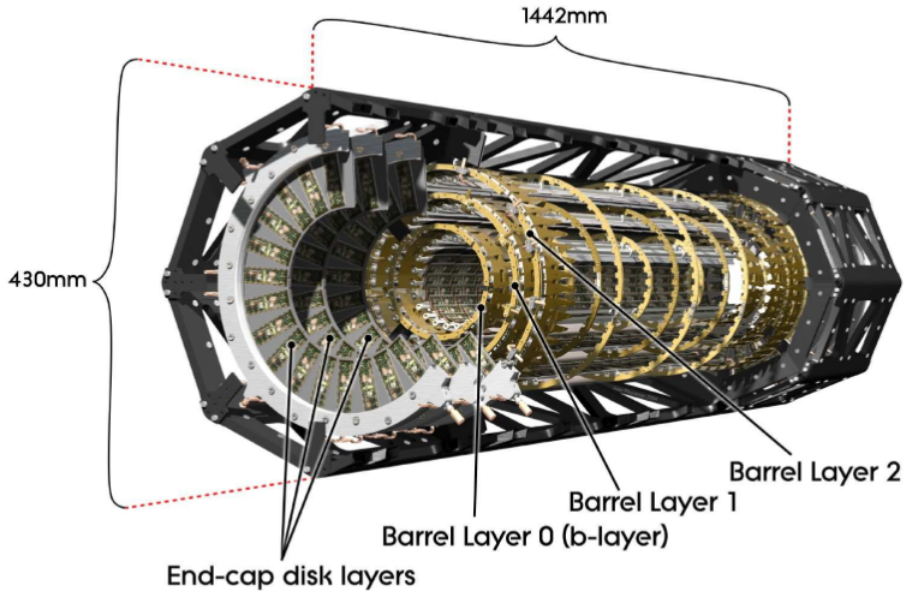


Figure 11: “A schematic view of the active region of the pixel detector consisting of barrel and endcap layers” [14]

2.3.2 Silicon Microstrip Trackers

The Silicon Microstrip Trackers (SCTs) operate with a similar principle as the pixel detectors, but have an effective operating voltage determined by the effective doping level, and their leakage current also increases linearly with radiation dose. Initially the operating

voltage was 150 V, but decreases up to 250 to 350 V to compensate for the radiation dose after 10 years. The 15912 SCT sensors use p-in-n, with each sensor having a thickness of $285 \pm 15 \mu\text{m}$ and a pitch of $80 \mu\text{m}$.

2.3.3 Transition Radiation Tracker

The Transition Radiation Trackers (TRT) make up the outermost region of the inner detector, and Fig. 5 details the dimensions of the extent of the TRT's envelope. Transition Radiation is the radiation emitted by a relativistic particle as it traverses through an interface for two materials with different permittivities. Each TRT is a 4 mm polyimide drift tube, created by two $35 \mu\text{m}$ multi-layer films bonded back-to-back [12]. A $25 \mu\text{m}$ thick polyimide film has one side laminated with a $0.2 \mu\text{m}$ of Al with another $5-6 \mu\text{m}$ layer of graphite [12]. Then the other side of the film has $5 \mu\text{m}$ of polyurethane to heat fuse the tube together at 200°C . The inside the tube is filled with a gas composed of 70% Xe, 27% CO_2 , and 3% O_2 . The anode is composed of $31 \mu\text{m}$ diameter cylinder of tungsten wire positioned at the center of the drift tube, and coated with $0.5 - 0.7 \mu\text{m}$ of gold. After fabrication, the tubes were cut to a 144 cm length for the barrel and 37 cm length for the end-cap region. The barrel straws are read out at each end of the tube, so the middle of the tube is insulated with a 6 mm glass layer which creates a 2 cm spot where the element is not sensitive to incident tracks. The anode is grounded and connected to the front end electronics, while the cathodes are held at -1530V . Minimizing the sag in the straw is crucial for accounting for the error in the position measurements, so the straws are mechanically supported by carbon fibers [12].

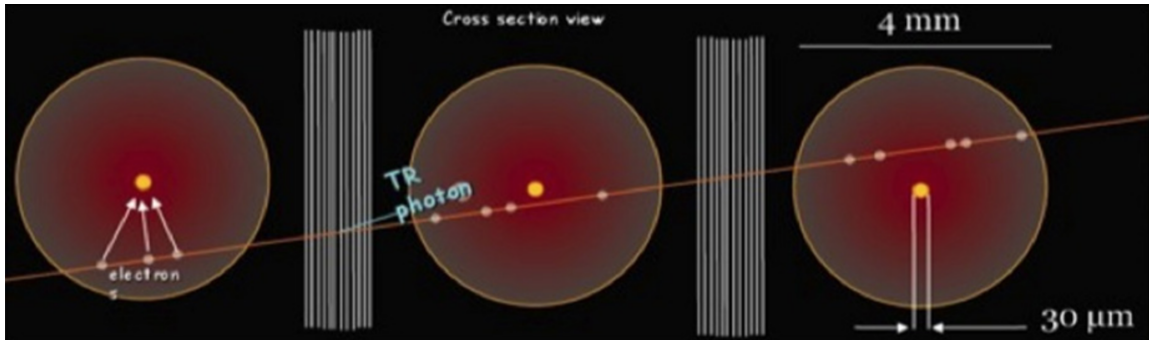


Figure 12: Principle of operation for the TRT [21]

An incident particle traversing through a straw ionizes the gas molecules to free electrons and free positive ions. The electrons accelerate through the electric field to the anode, and these electrons in turn will ionize other ions to create a gain of 2.5×10^4 . Since the anode is read out at both ends of the wire, this provides a drift time measurement from the difference of arrival times between the two ends of the wire. The time resolution is approximately a nanosecond, which corresponds to a spatial resolution of about 100 microns.

An outgoing particle will hit on average 36 of the TRT tubes, to improve the momentum measurement in the inner detector. During its lifetime, a straw detector can track 10^{15} particles, and a total integrated charge of 1000 C, which corresponds to about 20 years of

the LHC’s operation. The ATLAS inner detector has 12000 of these straws in the endcaps and 52544 straws in the barrel, yielding a total of 351 thousand read–out channels. Although the Silicon trackers need to be cooled between -5 to -10°C , the TRTs operate at room temperature.

2.4 ECAL

Calorimetry literally means “heat measurement” because the incident particle interacts with the material in the detector to form a shower of particles which are then decelerated through the material and the absorbed energy is measured to reconstruct the energy of the original particle. The ATLAS calorimeter is divided into two parts, the electronic calorimeter (ECAL) and the hadronic calorimeter (HCAL). The ECAL is for electronic interactions, and has higher precision than the HCAL which reconstructs the particles interacting by the strong force.

2.4.1 Sampling vs. Homogenous Calorimeters

For an electromagnetic shower to develop, incident electrons (and positrons) will emit a photon through Bremsstrahlung approximately in the distance of a *radiation length*

$$X_0 = \frac{716.4 \text{ g} \cdot \text{cm}^{-2} A}{Z(Z+1) \ln \frac{287}{\sqrt{Z}}} \quad (2.2)$$

where A is the number of nucleons in the material that the incident particle is passing through and Z is the atomic number, or number of protons in the atom of interest. Then the photons will in turn pair produce electrons and positrons when traveling a distance of $\frac{9}{7}X_0$. This showering phenomena will continue until the average particle energy decreases to below the *critical energy*, $E_c = \frac{610 \text{ MeV}}{Z+1.24}$. The hadronic showers are characterized by the *interaction length*, $\lambda = 37.8A^{0.312} \text{ g} \cdot \text{cm}^{-2}$, the average distance that an incident particle travels before undergoing a nuclear interaction.

There are two different calorimeters that can be used measure the incident particles energy. In a *sampling calorimeter* the calorimeter is created such that part the calorimeter is divided into scattering and absorbing slabs, shown in Fig. 13. The scattering slabs use a high Z material so that the radiation length is decreased, thus allowing the shower the develop more rapidly in this region. Then the energy is deposited in the absorbing region of the calorimeter. The final energy is then written as the energy deposited in the absorbing region divided by a scale factor, $f_{\text{sampling}} = \frac{E_{\text{visible}}}{E_{\text{deposited}}}$. A sampling calorimeter allows you to contain the shower in a smaller detector to help minimize the cost of the experiment. However, one of the downsides of this procedure is that

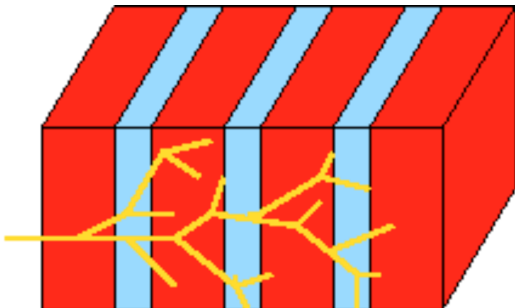


Figure 13: Schematic illustrating how a *sampling calorimeter* causes an incident particle to form a shower more quickly. [32]

the sampling method is not as precise because only a fraction of the energy deposited is measured, and fluctuations proportional to \sqrt{E} for Poisson statistics will introduce extra errors into t measurements.

To circumvent this problem, a *homogenous calorimeter* could also be used, where the whole calorimeter is an active volume that can be used to read out the data. A homogenous calorimeter is only useful for an ECAL because since the hadronic calorimeter has a much longer splay of particles in the shower, it no longer becomes monetarily feasible to contain all of the particles in a homogenous calorimeter. To see this, we can look at the approximate formulas for the *radiation length* and *interaction length*, $X_0 \sim \frac{A}{Z^2}$, and $\lambda \sim A^{1/3}$. Since Z is approximately $\frac{1}{2}A$, this means $\frac{\lambda}{X_0} \sim A^{4/3}$, a number that can be as large as 30 for high Z materials such as lead, and it is not too expensive to build a detector this large.

2.4.2 Liquid Argon Detector

The ATLAS ECAL is a sampling calorimeter arranged in an accordion structure, as shown in Fig. 14. Lead was the high Z material ($Z = 82$) used to create the shower, while the energy is measured in liquid argon, a low Z material ($Z = 18$). As Fig. 14 illustrates, the folding angle decreases as the radius (measured out from the interaction point) increases. The folding angle varies between $90^\circ - 67^\circ$ to keep the LAr sampling region width approximately constant at 2.1mm between the absorbers.

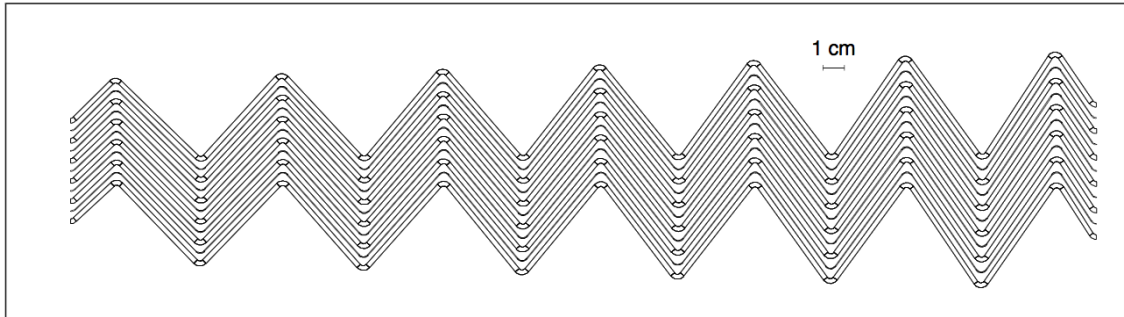


Figure 2-21 Transverse section through the active part of the barrel EM calorimeter (see also Figure 2-iii).

Figure 14: Accordion sampling structure for calorimeter. [24]

The LAr scintillators are read out with wave-length shifting photosensors. As is illustrated in Fig. 15, this type of a detector lends itself naturally to a tower structure with the modules forming wedges pointing back to the interaction point. This makes it easy for a particle's shower to be contained within a few modules or cells. The segmentation in $\Delta\eta \times \Delta\phi$ is 0.025×0.1 in the pre-sampler region, 0.0031×0.1 in the strips, 0.25×0.25 in the main region, and 0.5×0.025 in the back region. This yields an energy resolution of 10-12% $\text{GeV}^{-1/2}$.

2.4.3 GEANT 4 Simulations

Before building the detector, simulating the design in GEANT 4 is an important aspect of the design to test how well these elements might be expected to perform for the physics

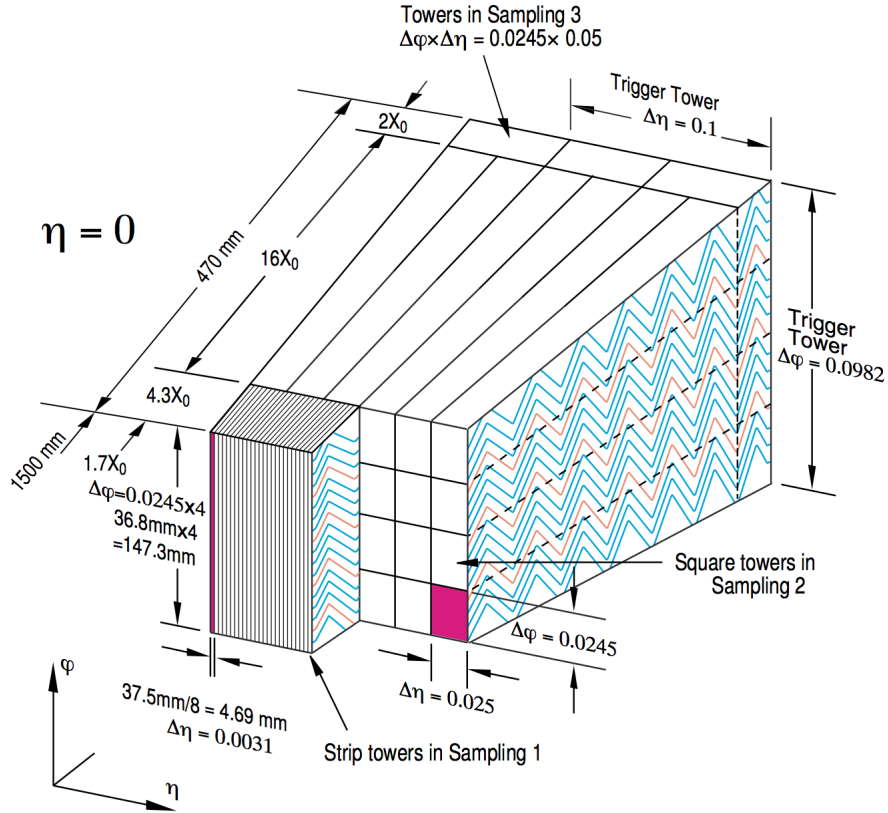


Figure 15: Wedge showing the accordian structure for the liquid Argon portion of the calorimeter. [24]

processes of interest. In Fig. 16, a cross-section of the ATLAS detector to the ECAL as simulated in GEANT 4 is shown.

To reconstruct the energy, first each cell is filled with a simulation for energy from a physics event, which can include pile-up. There is one matrix for each region of uniform granularity. Then the energies are summed based on calorimeter depth, and a search for clusters above a certain threshold is conducted by looking for a local maximum in some $\Delta\eta \times \Delta\phi$ window. This window size will need to be optimized in the jet-finding algorithm for the various clusters to minimize the affects of noise and pile-up. The optimization for this cut will depend on the luminosity. Finally, these “fired” cells are used to find the position and energy of the shower, where ϕ is corrected for due to the accordion shape, and the z is found from extrapolation from the η of the impacted cells [23].

The calorimeter measures the energy after the momentum has already been measured by the ID. Therefore, it is crucial that the inner detector have as few radiation lengths as possible to minimize effects of pair production and Bremsstrahlung that occur before the energy measurement even starts.

In Fig. 17, the amount of material (in radiation lengths) before the calorimetry is shown, dominated by the part of the material from the pixel, silicon strips, and TRT

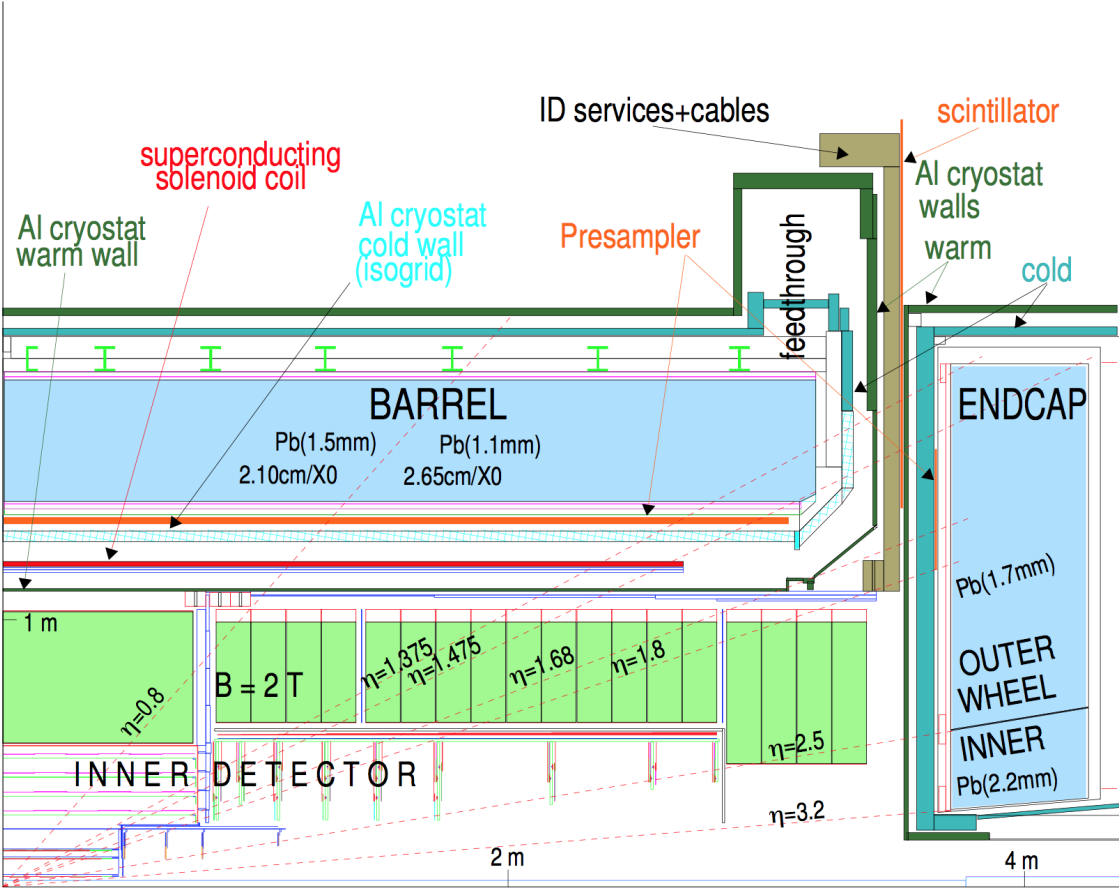


Figure 16: Detector simulation for a GEANT 4 simulation. [23]

components discussed in Section 2.3. Other material in front of the calorimeter comes from the cooling systems and solenoid surrounding the inner detector. The maximum at $\eta = 1.47$ is due to the overlap of components between the barrel and endcap regions, and the other local maximum at $\eta = 2.47$ is due to the overlap of components between the endcap and forward regions. Ideally, the ID material should be an insignificant fraction of the inner detector length, because when the material is an entire radiation length, half of the incident photons will already have pair-produced in the ID. However, as can be seen in Fig. 17, the amount ID material is not always an insignificant fraction of the material, so the next best plan is to try to account for any energy loss before the particle reaches the calorimetry.

One way to account for energy loss is by noticing that the Lorentz force $\vec{F} = q\vec{v} \times \vec{B}$

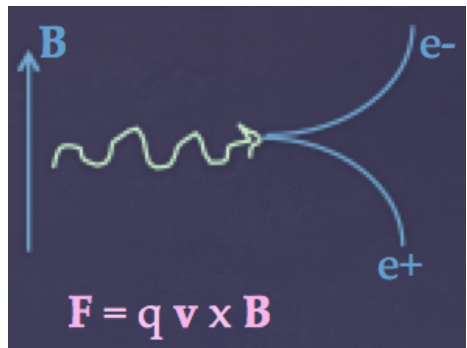


Figure 18: Pair production skewed by Lorentz force.

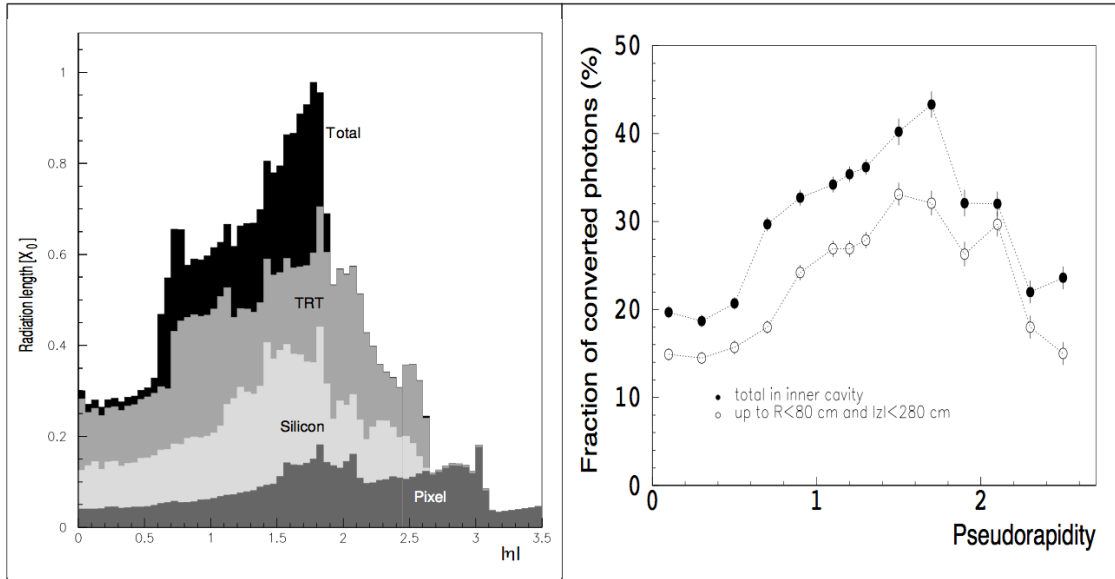


Figure 2-24 Material distribution in the inner cavity as a function of rapidity.

Figure 2-25 Fraction of photons converted in the inner cavity (closed symbols) and in the region where the conversions can be efficiently identified (open symbols), as a function of rapidity.

Figure 17: ID radiation lengths. [23]

will cause the an electron-positron pair to spread away from each other in the azimuthal direction. To correct for this phenomenon, assymmetric $\Delta\eta \times \Delta\phi$ windows can be used to allow an elongated $\Delta\phi$. In Fig. 19 it can be seen in the middle sampling region for electrons and converted photons, the $\Delta\eta \times \Delta\phi$ window is 7×3 cells, lopsided to account for this effect. The only downside is that a larger window makes it harder to reject background due to noise and background.

Table 2-2 Number of cells of the middle and back samplings used in the electromagnetic cluster for various particles and energies.

Particle type	Energy (GeV)	Middle sampling $\Delta\phi \times \Delta\eta$	Back sampling $\Delta\phi \times \Delta\eta$
Unconverted photons	< 100	5×3 cells	3×2 cells (used only for $E > 50$ GeV)
Electrons and converted photons	< 100	7×3 cells	3×2 cells (used only for $E > 50$ GeV)
Electrons and photons	> 100	5×5 cells	5×3 cells

Figure 19: Table for the number of cells used for clustering. [23]

To correct for the energy loss in front of the detector, the presampler allows the energy to be sampled just before the calorimeter to apply a weighting factor to estimate the energy

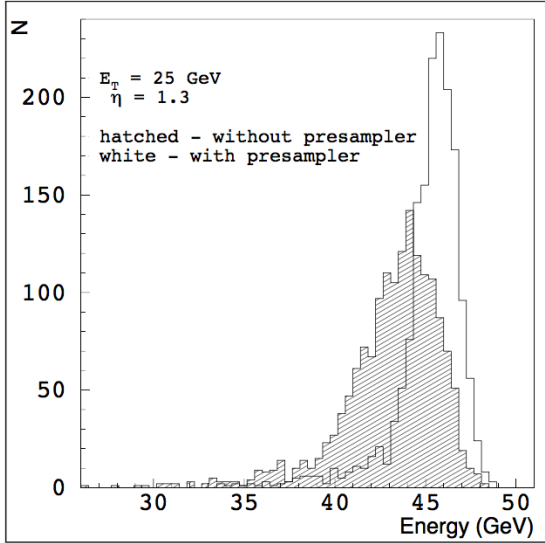


Figure 2-23 Energy spectra reconstructed in the EM calorimeter for photons of $E_T = 25$ GeV at $\eta = 1.3$ with (white histogram) and without (hatched histogram) adding the energy in the presampler.

Figure 20: Simulation demonstrating how including a presampler allows better energy reconstruction [23].

lost upstream of the calorimeter. The total energy is then

$$E_{tot} = w_{glob} (w_{ps} E_{ps} + E_{str} + E_{mid} + E_{back}) \quad (2.3)$$

where w_{glob} is a *global* weighting factor, w_{ps} is a weighting factor for the presampler, E_{ps} is the energy measured in the presampler, E_{str} is the energy measured in the strip towers, E_{mid} is the energy in the middle sampling region, and E_{back} is the energy measured in the back sampling region. In Fig. 20, the energy reconstruction for two 25 GeV photons at $\eta = 1.3$, where the passive material in front of ECAL is $\sim 3.9 X_0$. The hatched bell curve shows that the reconstructed energy distribution is skewed to the left, while when the $w_{ps} E_{ps}$ term is included, the Gaussian distribution peaks closer to the true value of 50 GeV, and has a smaller standard deviation as well.

In Figure 21 the $E_{reconstructed} / E_{incident}$ is plotted as a function of η . The reconstructed energy drops to much less than 1 at $\eta = 1.47$, due to the excess of passive material shown in Fig. 17. The presampler is not the only energy reconstruction factor, as the scintillator, located between the cryostat and the endcap. The scintillator detects the Cherenkov radiation emitted by particles traveling faster than the speed of light in the material, $v = \frac{c}{n}$, where n is the index of refraction. The angle of the Cherenkov radiation can be used to find the particle's speed which can be used to calculate the particle's energy. In Fig. 22, the energy a 30 GeV electron deposits in the ECAL is shown as a function of the energy deposited in the presampler and the scintillator. The closed squares show how the energy is reconstructed before the energy desposition in the scintillators and presampler is included. As the energy in the presampler or scintillator increases, the the reconstructed energy

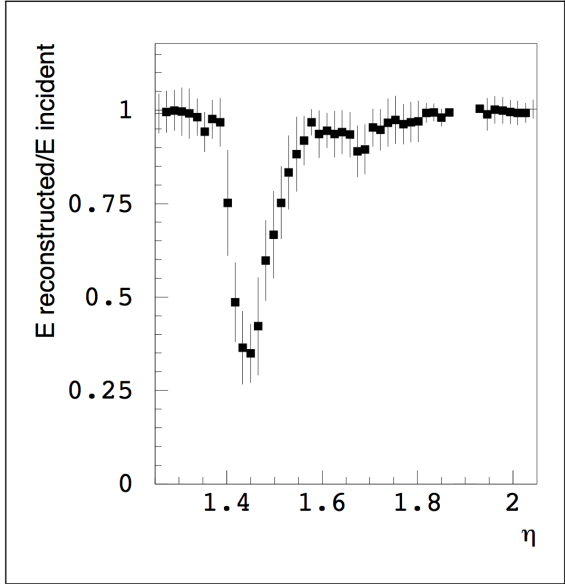


Figure 2-46 Ratio between the energy reconstructed in the EM calorimeter (in a 3×7 cell cluster) and the incident energy as a function of rapidity in the barrel/end-cap transition region for electrons of $E=30$ GeV. The error bars give the r.m.s. spread on the reconstructed energy.

Figure 21: Reconstruction of the energy in the ECAL [23].

decreases. However, because the trend is linear, a correction factor can be applied, as shown by the open squares. In Fig. 23, when both these affects are taken into account, the $E_{\text{reconstructed}} / E_{\text{incident}}$ versus η is plotted, and the uniform accuracy over a change of η values is recovered, although the error bars are significantly larger for $\eta = 1.47$, since this is the region where any error in the weighting factors from the scintillator and presampler will dominate.

Finally, because one of the main physics goals of the LHC was to discover the Higgs boson, the simulations were conducted to see how this algorithm for energy reconstruction could allow detection of the Higgs to the two photon or four electron final state. Because these graphs were made before the Higgs was actually discovered, guesses for the Higgs mass were used. In Fig. 24, the invariant mass of a 100 GeV Higgs decaying to two photons is reconstructed. A sample of 3500 $H \rightarrow \gamma\gamma$ events was generated with the two electromagnetic clusters having cuts for the leading $p_T > 40$ GeV, and the subleading $p_T > 25$ GeV, and both clusters were required to be within $|\eta| < 2.4$. The gaussian fit to the simulation data shows that the distribution does peak at 100 GeV, and the width of this gaussian comes primarily from the sampling term, since the yellow histogram, which contains at-least one converted photon dominates the error of the white histogram which includes all of the events.

An invariant mass of 130 GeV for the Higgs decaying to the four electrons through $HH^- \rightarrow ZZ^* \rightarrow e^+ e^- e^+ e^-$ is illustrated in Fig. 25, where Z^* denotes an “off-shell”

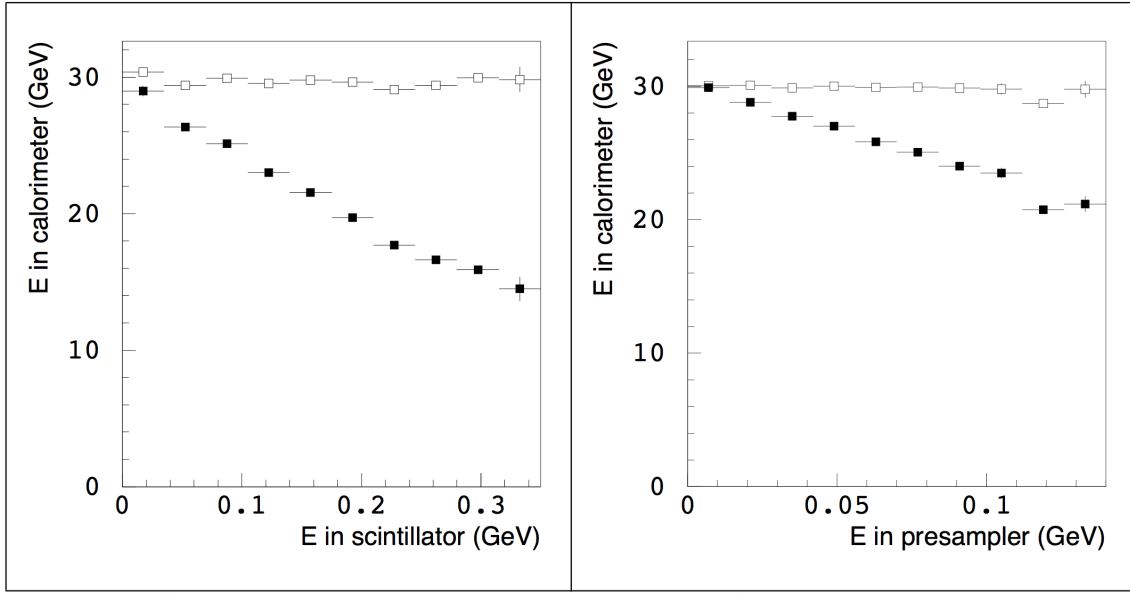


Figure 2-48 Calibrated energy reconstructed in the calorimeter as a function of the energy deposited in the scintillator for electrons of $E=30$ GeV at $\eta \sim 1.47$ before (closed symbols) and after (open symbols) correction.

Figure 2-49 Calibrated energy reconstructed in the calorimeter as a function of the energy deposited in the presampler for electrons of $E=30$ GeV at $\eta \sim 1.68$ before (closed symbols) and after (open symbols) correction.

Figure 22: Reconstruction of the energy in the ECAL [23].

Z boson because the sum of two Z bosons masses is not 130 GeV. The leading jet was required to have a $p_T > 20$ GeV, and the subleading jet was required to have a $p_T > 7$ GeV. These p_T cuts are lower even though the mass of the Higgs is higher than used in the di-photon final state because now there will be four energy clusters for the two electrons and two positrons, instead of the two from the di-photon final state. One of the Z's was required to be on-shell, with the reconstructed mass window within $m_{12} = m_Z \pm 6$ GeV, while the off-shell Z needed to have a mass $m_{34} > 20$ GeV. High energy (> 5 GeV) bremsstrahlung photons decrease the energy resolution, and we can see this in Fig. 25 because the standard deviation is larger in the second figure that included high energy bremsstrahlung electrons.

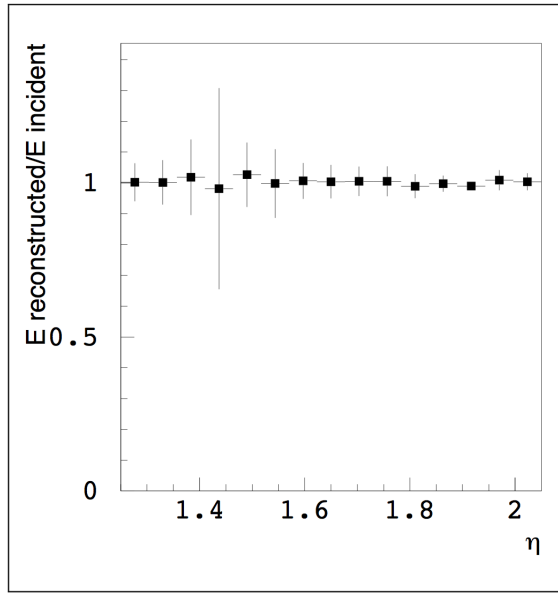


Figure 2-50 Ratio between the energy reconstructed in the EM calorimeter and the incident energy as a function of rapidity in the barrel/end-cap transition region for electrons of $E=30$ GeV, after the energy released in the scintillator and presampler is added. The error bars give the r.m.s. spread on the reconstructed energy.

Figure 23: Reconstruction of the energy in the ECAL [23].

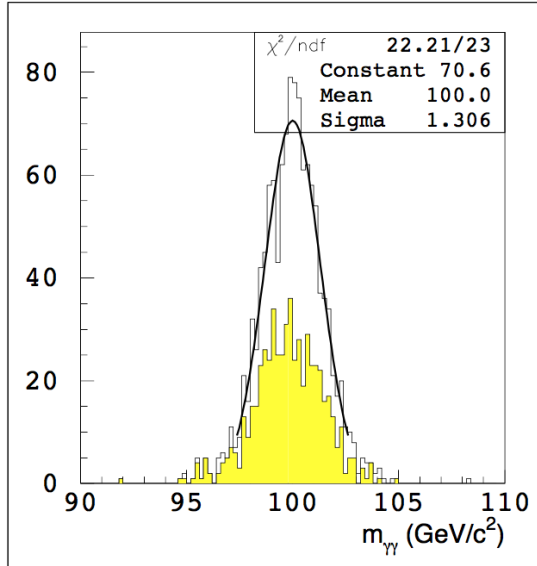


Figure 2-68 Two-photon invariant mass reconstructed in the EM calorimeter for $H \rightarrow \gamma\gamma$ events with $m_H = 100$ GeV at high luminosity. The white histogram is for all events, the shaded histogram for events containing at least one converted photon.

Figure 24: $H \rightarrow \gamma\gamma$ [23].

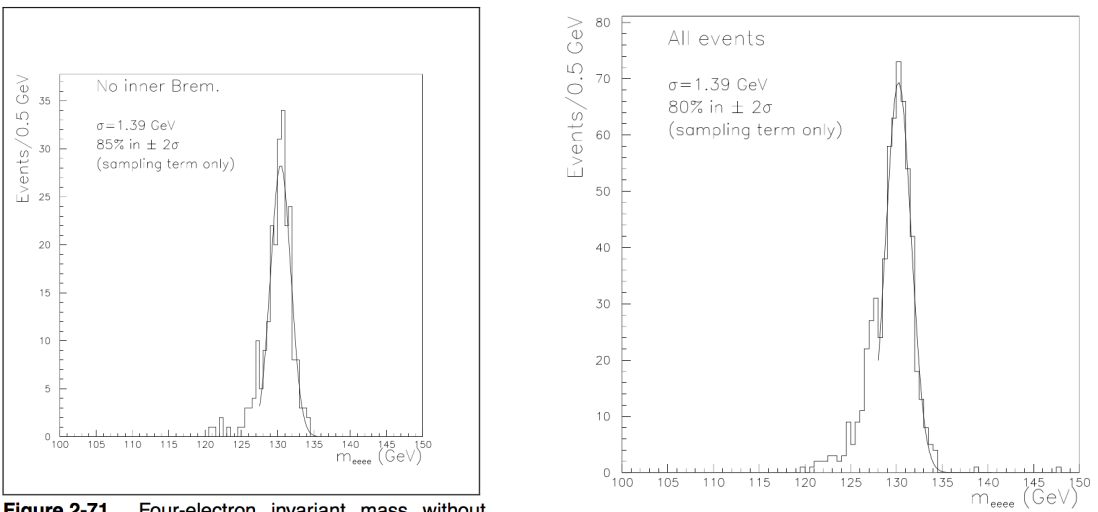


Figure 2-71 Four-electron invariant mass without inner bremsstrahlung contribution.

Figure 25: Reconstruction of invariant mass for a 130 GeV Higgs with $H \rightarrow 4 e-$ decay mode [23].

2.5 HCAL

The hadronic calorimeter (HCAL) is the layer right outside of the ECAL, and measures the development of the jets generated by the strong force. Although the ECAL system could be used to measure the development of the hadronic showers as well, the HCAL system's coarser granularity decreases the monetary cost in covering this larger volume. It is divided into three parts: the tile calorimeter, the LAr hadronic end-cap calorimeter, and the LAr forward calorimeter, as shown in Fig. 26.

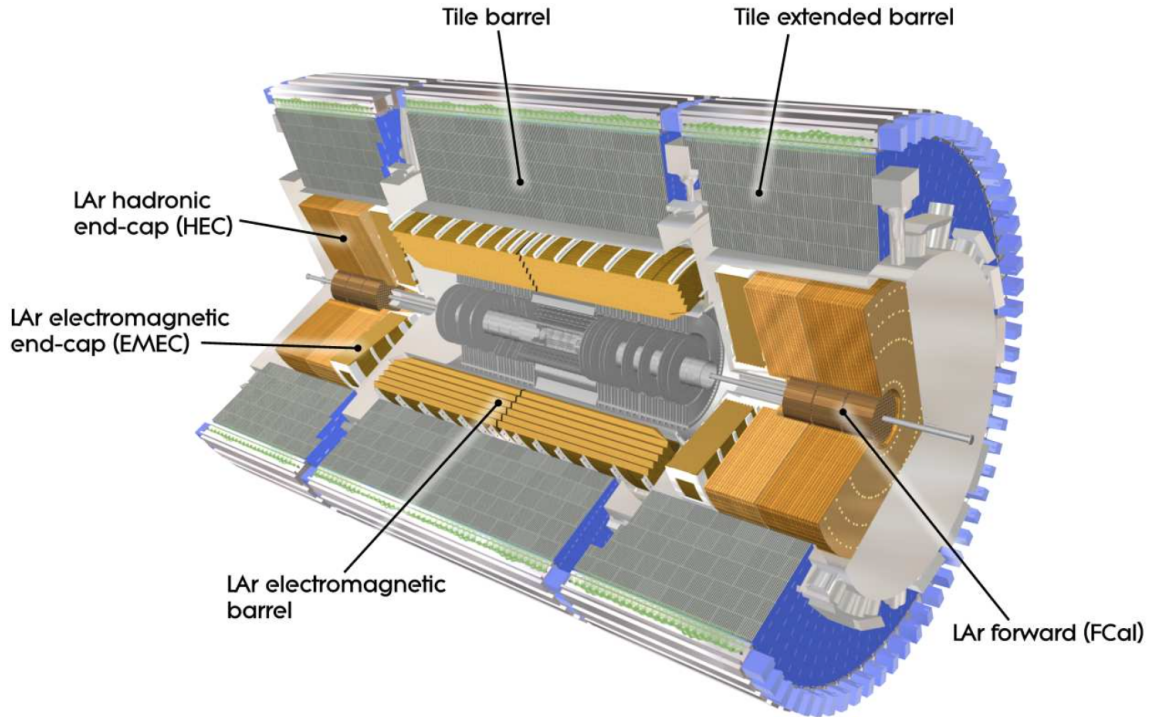


Figure 26: Calorimeter system at ATLAS [12].

2.5.1 Tile Calorimeter

The tile calorimeter is the envelope just outside ECAL with inner radius 2.28m, outer radius 4.45m. The coverage of the barrel with $|\eta| < 1.0$, while the extended barrels cover $0.8 < |\eta| < 1.7$. It is a sampling calorimeter with a steel absorber and scintillating tiles read out with wavelength shifting fibers and photomultiplier tubes. Azimuthally divided into 64 modules, the barrel is segmented into three regions at the *interaction lengths* (λ) 1.5, 1.8, and 4.25, while the extended barrel has 1.5, 2.6, and 3.3λ depth segmentation. At $\eta = 0$, the HCAL has a 9.7λ depth [12].

2.5.2 LAr hadronic end-cap calorimeter

The LAr hadronic end-cap calorimeter has two wheels per endcap just behind the ECAL endcap calorimeter and housed within the same LAr cryostats. The wheels segmented into two depth segments, 25 mm parallel copper plates for the wheels closest to the interaction

point, and 50 mm plates for the wheels farther from the interaction point. The wheels are divided into 32 wedges, with inner and outer radii 0.475m and 2.03m, respectively. The copper plates filled with LAr as the active sampling volume [12].

2.5.3 LAr forward calorimeter

The forward calorimeter cover $\eta > 3.1$ and is approximately 10 interaction lengths deep. Each side has three modules, the first of copper for electronic measurements, and the second two of tungsten for hadronic measurements.

2.6 Muon Spectrometer

A good tracking system is vital for determining the momentum of a charged particle from its radius of curvature in a magnetic field, $R = \frac{p_T}{qB}$. A more massive object moving at the same velocity will have a larger transverse momentum, and therefore a larger radius of curvature. Since the muon is 200 times heavier than an electron, it can be difficult to have tracking system that can accurately measure the momentum for relativistic muon and electron, so the muon detection system is separated to measure the p_T for a broad range of muon energies.

The muon detector is also a gas detector (like the TRT), so will operate according to similar principles. The components of the muon spectrometer are detailed in the subsections below, while the parameters for the coverage and number of channels for are listed in Fig. 27.

2.6.1 Toroidal Magnets

The muons are detected through the deflection of their tracks bent by a 4 T magnetic field. There are three large air–core toroids, and each of these 3 toroids has 8 coils. The particles of interest that reach this portion of the detector are muons and neutrinos, but only the muons will be detected because the electrically neutral neutrinos are not be deflected by the magnetic field. Background for the muon spectrometer are photons and neutrons with energies below an MeV and 100 MeV, respectively [22]. The Muon tracker is a gas detector, and operates under a similar principle to the inner detector. Magnetic field is designed to be transverse to muons’ flight direction to minimize multiple scattering. The magnets are housed within cryostats to keep them below the critical temperature for superconductivity. Inside these magnets are the muon chambers divided into three cylindrical chambers about the beam axis in the barrel region, while the transition and end–cap regions arranged as disks, also divided into three chambers [12].

2.6.2 Monitored Drift Tubes

The Monitored Drift Tubes (MDTs) are drift chambers that provide precision measurements. Each tube is made of aluminum with a 3 cm diameter and length between 0.9 and 6.2 m. The tube is filled with a 93% Ar, 7% CO₂ gas mixture, at a pressure of 3-bar [22]. It has a gain of 2×10^4 [22], same as the TRT drift chambers Section 2.3.3. The accuracy for single muon events is 100 μm , while the accuracy for multi-muon events is 50 μm [22]. To control the accuracy, the sag of the wires is minimized by three kinematical mounts placed

Monitored drift tubes	MDT
- Coverage	$ \eta < 2.7$ (innermost layer: $ \eta < 2.0$)
- Number of chambers	1088 (1150)
- Number of channels	339 000 (354 000)
- Function	Precision tracking
Cathode strip chambers	CSC
- Coverage	$2.0 < \eta < 2.7$
- Number of chambers	32
- Number of channels	31 000
- Function	Precision tracking
Resistive plate chambers	RPC
- Coverage	$ \eta < 1.05$
- Number of chambers	544 (606)
- Number of channels	359 000 (373 000)
- Function	Triggering, second coordinate
Thin gap chambers	TGC
- Coverage	$1.05 < \eta < 2.7$ (2.4 for triggering)
- Number of chambers	3588
- Number of channels	318 000
- Function	Triggering, second coordinate

Figure 27: Main parameters for the Muon Spectrometer. The values in parentheses refer to the configuration from 2009 [12].

strategically to minimize distortion due to the support, as shown in Fig. 28b. There are a total of 1174 MDTs positioned in the barrel of the ATLAS detector, $|\eta| < 2$.

2.6.3 Cathode Strip Chambers

For larger pseudorapidities ($2 < |\eta| < 2.7$), Cathode Strip Chambers (CSCs) are used for their higher granularity in the endcap region [12]. This is a multi-wire proportional chamber (MWPC) with strip read-out with a sense wire pitch of 2.54 mm and a read-out strip pitch of 5.08 mm resulting in a 60 μm track resolution [22].

2.6.4 Level I Muon Trigger

Level 1 trigger looks for muons with HIGH p_T pointing back to the interaction point [22]. There are two different cut-offs for the muon p_T , 6 GeV and 20 GeV for the respective low and high p_T thresholds [22]. Triggers provide information about the bunch-crossing rate, thresholds for the p_T , and the muon's coordinates orthogonal to the beam pipe [12]. The $|\eta| < 2.4$ coverage for the trigger is narrower than the coverage of $|\eta| < 2.7$ for the precision muon tracking (see Section 2.6.3), so that if a muon triggers on the edge of the triggering system, its trajectory can be followed out to a larger opening angle.

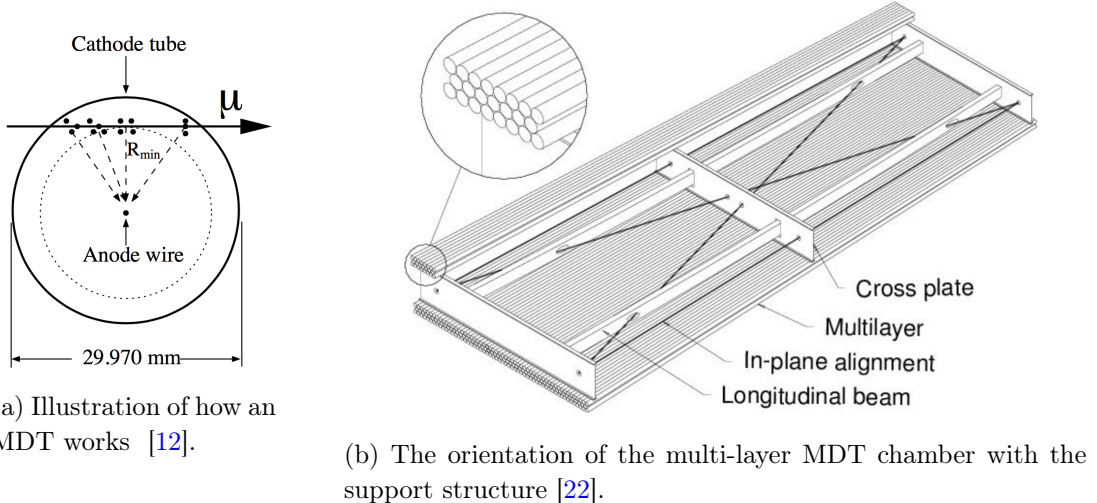


Figure 28: Monitored Drift Tubes: MDTs

Because of the different rates for muons in different regions of the detector, different subsystems are used for different regions of the muon detector. In the barrel region Resistive Plate Chambers (RPCs) are used, operated in avalanche mode, which allows large current outputs to be generated by a slight current input [22]. Each chamber has two gas-volumes read-out with four planes of read-out strips to provide a read-out on each end for each gas volume. The detector uses two RDCs surrounding the innermost MDT layer tuned to detect the low- p_T threshold, and then a third outermost RDC tuned to detect the high- p_T threshold as illustrated in Fig. 29 [22]. The time-resolution of these devices is 2 ns. In endcaps, Thin Gap Chambers (TGCs) are operated in saturation mode, which gives a constant gain for each input current, or an output linearly proportional to the input [22]. The low and high momentum resolutions are $\sim 30\%$ and $\sim 20\%$, respectively [22]. The low- p_T muon measurement is limited by the multiple-scattering and energy-fluctuations, while the high- p_T muon resolution is limited by the interaction regions length [22]. Single measurement accurate to 30 microns, for multi-muon final-states, it's a few mm [12].

2.7 Forward Detectors

The forward detector at ATLAS covers pseudorapidities $|\eta| > 8.2$, and has three subsystems: two to measure the luminosity and the last one for heavy-ion studies conducted when the collider accelerates with lead nuclei at $\sqrt{s} = 5$ TeV. LUCID (LUminosity measurement using Cerenkov Integrating Detector) is located ± 17 m from the interaction point, and is the primary online luminosity detector for ATLAS. ALFA (Absolute Luminosity For ATLAS) is located ± 240 m, and uses scintillating fibers as another measure for the luminosity, with these fibers extending as a millimeter from the beam pipe. Finally, ZDZ (Zero-Degree Calorimeter) lies ± 140 and has alternating layers of quartz rods and tungsten plates for detecting neutral particles at pseudorapidities $|\eta| > 8.2$ [12].

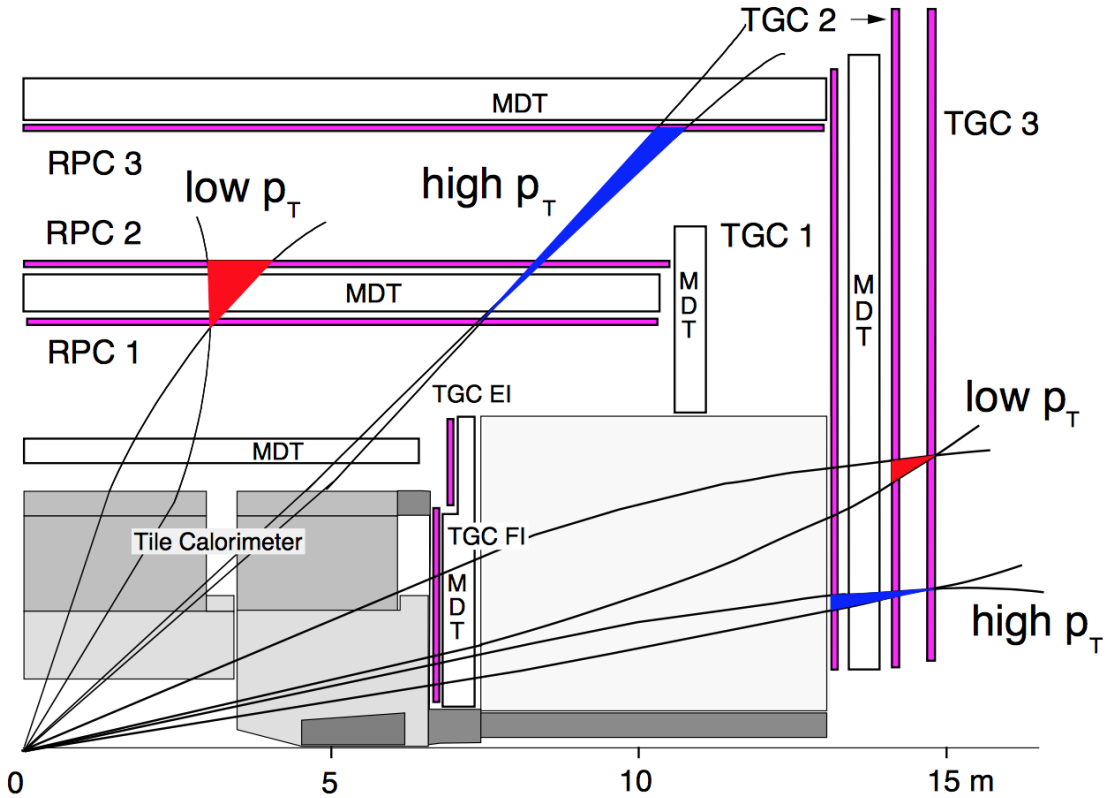


Figure 29: Muon trigger [22].

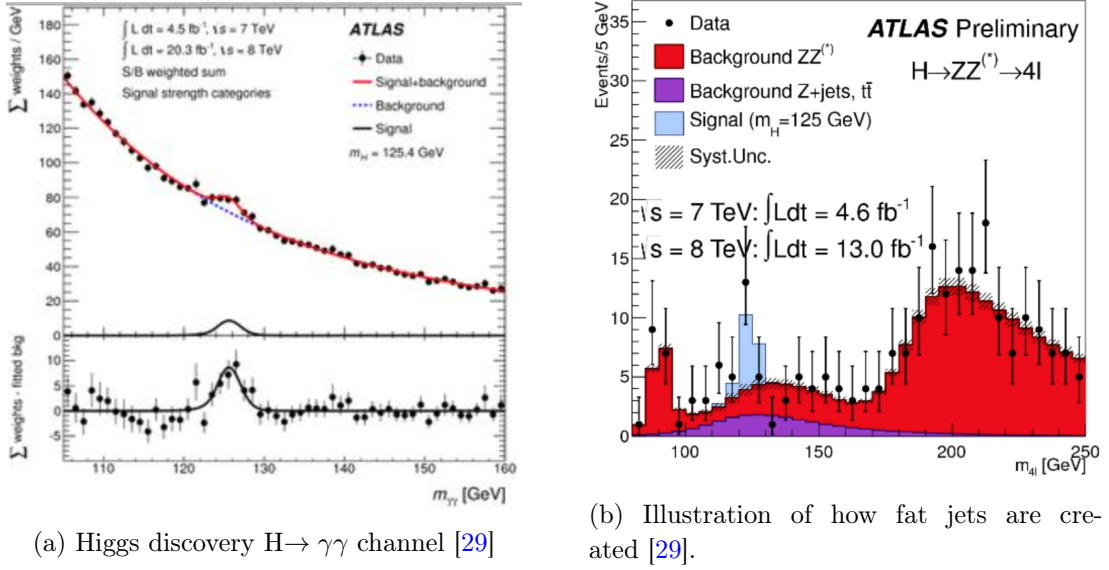
3 Higgs Decay Modes

The Higgs discovery was made using the “clean” decay modes $H \rightarrow \gamma\gamma$ and the “golden channel” with a Higgs decaying to four leptons, displayed in Fig. 30 [29].

The cross-sections for the Higgs are given in Fig. 31. Although the $H \rightarrow \gamma\gamma$ and $H \rightarrow ZZ$ modes have low branching modes, they were used for the discovery mode because they involve channels that are clean depositing most of their energy in the ECAL and muon chambers for the leptonic decays, respectively. Now, that the Higgs has been discovered, the scientific community is interested in probing its properties, in particular it’s self-interaction by looking for di-Higgs decays. From Fig. 31, it is clear that to find more Higgs’s, elucidating the b-quark decay mode becomes extremely important. It’s difficult to discriminate b quarks from background in ATLAS because the b quark decays via the strong force, and since the LHC is a hadronic collider, there is a lot of QCD background as well, so isolating the b-quark jets with sufficient resolution becomes critical.

4 Jets

As mentioned in section 1, a simple model for how a jet can be initiated is given by the (insert name) Model. (Go into the simple model to understand shower of particles (from



(a) Higgs discovery $H \rightarrow \gamma\gamma$ channel [29]

(b) Illustration of how fat jets are created [29].

Figure 30: ATLAS figures for the channels used for the 2012 Higgs boson discovery

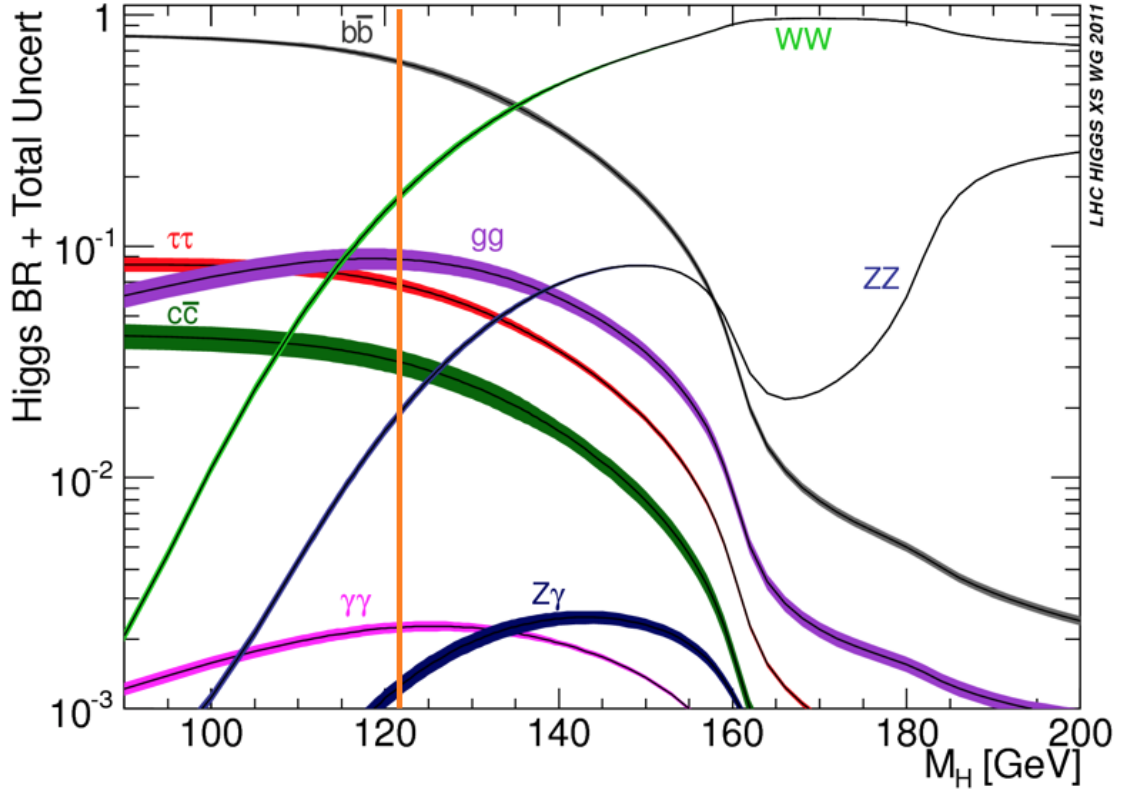


Figure 31: Branching ratios for the various decay channels of the Higgs, where the orange line at 125 GeV was added to emphasize the true branching ratios.[3]

Ye's class))

The detector produces energy by “absorbing” the particles, and to then cluster the deposited energy into a jet, the anti-k_T algorithm is used (just cite).

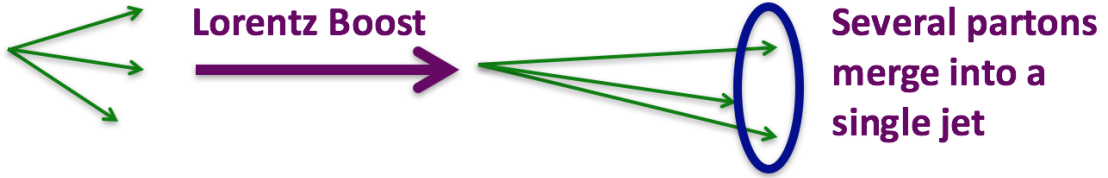


Figure 32: ATLAS figures for the channels used for the 2012 Higgs boson discovery

Since the protons are not point-like, the colliding constituent particles may not have equal p_T in the lab frame. However, by definition, the net momentum will be zero in the center of mass frame. Therefore, one can create a heavy (TeV) resonance at rest in the CM frame, but when applying a Lorentz transform back into the CM frame means that the decay products can become highly collimated. At this point, the decay products can no longer be resolved, and it is more efficient to clump the decaying jets individually, to combine them into two fat jets (cite your REU paper?) [?]. The constituent parts of the “fat jet” can still be identified and are called *subjets*.

4.1 b tagging

Current methodology for detecting b quarks is to use a procedure known as “b tagging” [?]. The b quark tends to combine with an anti-b, to create a b meson, which has a lifetime of 1.5 ps [34, 36], and will travel about a mm in the detector for the relativistic meson. This path length is long enough that it can be measured inside the pixel detector. The signature for such an event is a vertex, and then a path approximately a few mm, and then another vertex, as shown in Fig. 33. Such a displaced vertex is identified by the impact parameter (IP) “the distance from the point of closest approach of the track to the interaction vertex” [36]. So a jet that originally had such a displaced vertex is used to identify b-jets in ATLAS. This b-tagging algorithm can be used for both resolved jets, or for the subjets inside a fat jet. The b-tagging algorithm is only 70% efficient [37], which means identifying two b-quarks this way is only 49% efficient, motivating the search for another method, i.e, the ECF method, suggested for a fat jet analysis, but used in this context for resolved jets.

The electromagnetic calorimeter has coverage out to $|\eta| = 3.0$, and the hadronic calorimeters have full coverage to $|\eta| = 5.0$, which the pixel detector only has coverage out to $|\eta| = 2.4$.

5 Energy Correlation Functions

In [33], the authors suggested to use Energy Correlation Functions, and in particular, two discriminating variables C_1 and C_2 to help discriminate the b-quarks from QCD background.

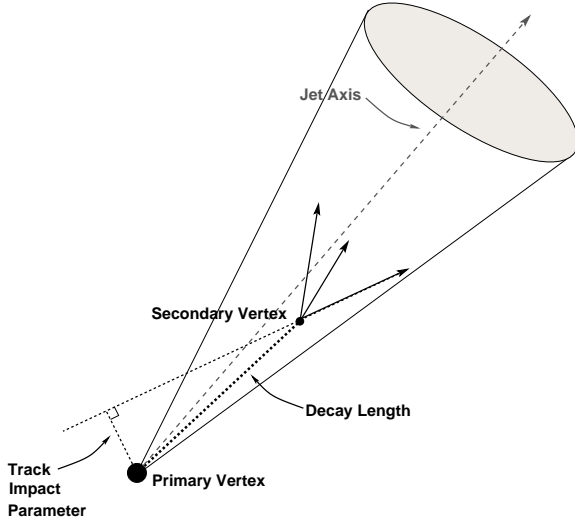


Figure 33: “A secondary vertex with a significant decay length indicates the presence of a long-lived particle in the jet” [35]

Below, the relevant information from this paper is summarized.

Before, N-subjettiness was used to detect the number of subjets in a larger jet (cite).

This paper “introduces generalized energy correlation functions that can identify N-prong jet substructure without requiring a subjet finding feature” [33].

The N-point ECF that they introduce is defined in Eq. (5.1).

$$ECF(N, \beta) = \sum_{i_1 < i_2 < \dots < i_N \in J} \left(\prod_{a=1}^N p_{T_{ia}} \right) \left(\prod_{b=1}^{N-1} \prod_{c=b+1}^N R_{i_b i_c} \right)^\beta \quad (5.1)$$

where J is the complete “fat jet” under consideration, $i_j, j \in \{1, \dots, N\}$ are label the N subjets in J , and

$$R_{ij}^2 = (y_i - y_j)^2 + (\phi_i + \phi_j)^2, \quad (5.2)$$

$$y_i = \frac{1}{2} \ln \frac{E_i - p_{zi}}{E_i + p_{zi}}, \quad (5.3)$$

Note, y_i is the rapidity, but since the rapidity becomes the pseudo-rapidity in the relativistic limit (as is the case at relevant analyses at the LHC), in my analysis, the rapidity in this definition, was replaced by the pseudo-rapidity (cite pseudo-rapidity definition from the ATLAS section).

So, for example, the definitions for the first few N-values which will be of interest to our analysis are

$$ECF(0, \beta) = 1 \quad (5.4)$$

$$ECF(1, \beta) = \sum_{i \in J} p_{T_i} \quad (5.5)$$

$$ECF(2, \beta) = \sum_{i < j \in J} p_{Ti} p_{Tj} (R_{ij})^\beta \quad (5.6)$$

$$ECF(3, \beta) = \sum_{i < j < k \in J} p_{Ti} p_{Tj} p_{Tk} (R_{ij} R_{jk} R_{ki})^\beta \quad (5.7)$$

If you try to construct an N-prong ECF with less than N constituents, the ECF will return 0. However, the algorithm to try to determine the number of subjets in a fat jet will not be 100% efficient at identifying the true number of b-jets, but realistically a fat jet with N-subjets should have $ECF(N+1, \beta)$ much smaller than $ECF(N, \beta)$. This motivates the use of $r_N^{(\beta)}$ defined as

$$r_N^{(\beta)} = \frac{ECF(N+1, \beta)}{ECF(N, \beta)} \quad (5.8)$$

We expect $r_N^{(\beta)}$ to be small for and $r_{N-1}^{(\beta)}$ to be large for an N-subjet system (?)

Finally, the authors defined the test-statistic C_N as a ratio [33]

$$C_N^{(\beta)} = \frac{r_N^{(\beta)}}{r_{N-1}^{(\beta)}} = \frac{ECF(N+1, \beta) ECF(N-1, \beta)}{ECF(N, \beta)^2} \quad (5.9)$$

For a jet with N subjets, C_N is expected to be significantly larger than C_{N-1} [33]

“ C_N effectively measures higher-order radiation from leading-order (LO) substructure” [33].

“If C_N is small and C_{N-1} is large, then we can say that a system has N subjets” [33].

(*) Could talk about *soft and collinear gluon emission* b/c a nice feature about this method is that the ECF is infra-red and collinear safe, but I don’t think this fact is relevant for this analysis?

5.1 C1 Discriminating Variable

$$C_1^{(\beta)} = \frac{ECF(2, \beta) ECF(0, \beta)}{ECF(1, \beta)^2} = \quad (5.10)$$

“At large values of β , wide-angle emissions are given greater weight, and at small values of β , collinear emissions are given greater weight” [33].

“Multiple emissions tend to increase the value of the observable C_1 , so for fixed C_1 must be suppressed. Likely to be more multiple emissions for gluons than quarks, so it “costs” more to accept a gluon jet” [33].

Note: “only beyond LL order does the discrimination depend on β ” [33], so the LO sample that I ran on should not depend on the β chosen at this point, though a future study with an NLO sample could optimize the β chosen for the study.

The authors MC analysis concluded that the quark-gluon discrimination increased as β decreased [33]. This is another motivation to choose the small β value.

- The optimization was already maximized for $\beta_{C1} = 0.2$ when $p_T \in [400, 500] GeV$, with $R_0 = 0.6$. Q: Should I redo the optimization for the b quarks in the resolved case?

A: Look at the paper, and see how much variation you can expect for different p_T .

5.2 C2 Discriminating Variable

The C_2 is useful for identifying 2 subjets in a fat jet, as is applicable to analyses with boosted W, Z, and H's. The identification process first applies a mass cut, and then uses C_2 as a further discrimination variable to reduce the QCD background.

Note “this tagging procedure is very sensitve to the ratio of jet mass to jet p_T ” [33].

“For jets with mass comparable to their transverse momentum, the mass is dominated by a single, relatively hard, perturbative splitting. So the QCD jets that can fake a boson are those with two relatively hard cores of energy surrounded by soft radiation” [33].

“The rejection rate (for QCD) increases as jet R_0 increases . . . [and] at small R_0 , [not the case when we’re calling the fat jet all of the detector], large β lead to the best discrimination” [33].

“Note: C_2 itself is only IRC safe with a cut on the jet mass” [33], but this is ok, because in the last step, I do implement a mass cut!

“The QCD jets C_2 increases dramatically, while the H bosons C_2 value stays closer to lower C_2 values” [33].

Q: Is this the same trend that I saw?? If not, could it be b/c I applied the C_1 cut before applying a C_2 cut?

A: ?

5.3 Applications to this analysis

- How we’re applying the “fat jet” to all of space to apply this same principal
- This method doesn’t rely as heavily on information from the tracker as the b-tagging algorithm does, so it can still detect Higgses in the forward region where the calorimeter extends, but not the pixel detector.

6 Results

First I reproduced the analysis for the C_1 variable, and then optimized the β for C_2 variable.

6.1 C1 Discriminating Variable

Maddie’s cut: $0.22 < C_1 < 3.2$

My cut: $0.2x < C_1 < 3.x$

- C.f. paper’s results

6.2 C2 Discriminating Variable

- beta optimization(?)

6.2.1 Likelihood function cuts

- Talk about Neeman-Pearson Lemma - Likelihood functions

6.2.2 Optimization of Bc2

- Talk about why the energy is so low
B mesons have preferential decays to semi-leptonic final states (30% - 40% of the time)
CITE FROM PDG.

The neutrinos lose energy into things you NEVER can reconstruct exactly!

7 Future Work

- Apply the jet energy corrections (it's an established software package in ATLAS)
- Control Sample of $HH \rightarrow b\bar{b}b\bar{b}$ MC
- Run on data

8 Acknowledgements

Everybody!

- Dr. Sekula for mentoring
- Feikert, Maddie for finding the ECF paper and implementing it in code.

References

- [1] "The Higgs boson." CERN, <http://home.cern/topics/higgs-boson>, accessed 11 April 2016.
- [2] "The Standard Model of Particle Physics." *Symmetry Magazine*.
<http://www.symmetrymagazine.org/standard-model/>, accessed 11 April 2016.
- [3] *Higgs Hunter*
- [4] P. W. Higgs, "Broken symmetries and the masses of gauge bosons," Phys. Rev. Lett. 13 (1964) 508–509. <http://link.aps.org/doi/10.1103/PhysRevLett.13.508>.
- [5] P. W. Higgs, "Spontaneous symmetry breakdown without massless bosons," Phys. Rev. 145 (1966) 1156–1163. <http://link.aps.org/doi/10.1103/PhysRev.145.1156>.
- [6] S. Weinberg, "A model of leptons," Phys. Rev. Lett. 19 (1967) no. 21, 1264–1266.
- [7] A. Salam, in Elementary Particle Theory, p. 367. Almqvist and Wiksell, Stockholm, 1968.
- [8] S. Dawson, "Introduction to electroweak symmetry breaking," arXiv:hep-ph/9901280 [hep-ph].
- [9] Y. Grossman. "Introduction to the Standard Model." *CERN Summer Student Lectures* 4 July 2014.
- [10] "The Nobel Prize in Physics 2013."
http://www.nobelprize.org/nobel_prizes/physics/laureates/2013/ Accessed 25 Dec 2015.
- [11] "The Large Hadron Collider." CERN, <http://home.cern/topics/large-hadron-collider>. Accessed 11 April 2016
- [12] G. Aad, E. Abat, J. Abdallah, *et al.*, "The ATLAS Experiment at the CERN Large Hadron Collider." Journal of Instrumentation, Vol. 3, August 2008.
- [13] CMS Collaboration. "Limits on the Higgs boson lifetime and width from its decay to four charged leptons." arXiv:1507.06656v2.

- [14] G. L. Aad, M. Ackers, F. A. Aleppo, *et al.*, “ATLAS Pixel Detector Electronics and Sensors,” *Jinst*.
- [15] S. Herrmann. “SLAC LCLS/SSRL Users meeting - Detector Workshop”: Conference Proceedings.
- [16] S. Zenz “How a Pixel Detector Works.” Imperial College London Blog.
<http://www.quantumdiaries.org/2008/07/25/how-a-pixel-detector-works>. Accessed 4 Oct. 2015.
- [17] S. Stapnes. “Detector Challenges at the LHC.” *Nature*, Vol. 448. 19 July 2007.
- [18] S. Sekula. “The Particle Family.” Introductory Public Lecture at the Deep Inelastic Scattering Conference. 26 April 2015.
- [19] R. Fernow. *Introduction to Experimental Particle Physics*. Cambridge University Press, 1986.
- [20] <https://portal.uni-freiburg.de/jakobs/dateien/vorlesungsdateien/wpf2hadroncollider/kap2c>. Accessed 2 Nov 2015.
- [21] “ATLAS TRT (Transition Radiation Tracker).”
<http://particle.mephi.ru/en/research/atlas/trt/>. Accessed 23 Dec 2015.
- [22] P. Sandro. “The Muon Spectrometer of the ATLAS Experiment.” ATLAS Note/Com.: ATL_COM-MUON-2003-005.
<https://palesti2.web.cern.ch/palesti2/Documents/SPsienaNote.pdf>. Accessed 23 Dec 2015.
- [23] Technical Design Report: ATLAS Calorimeter Performance, 1997,
<http://atlas.web.cern.ch/Atlas/TDR/caloperf/caloperf.html>. Accessed 2 Nov 2015.
- [24] Technical Design Report: Liquid Aragon, Ch 1 and Ch 6, 1996.
- [25] ATLAS Multimedium, The Electromagnetic Calorimeter,
<http://www.atlas.ch/multimedia/electromagnetic-cal.html>. Accessed 2 Nov 2015
- [26] M. Kado, ATLAS Collaboration. “Results with the Full 2015 Data Sample from the ATLAS Experiment.” Conference Proceedings, 15 Dec 2015.
<https://indico.cern.ch/event/442432/contribution/1/attachments/1205572/1759985/CERN-Seminar.pdf>. Accessed 25 Dec 2015.
- [27] J. Olsen, CMS Collaboration. “CMS 13 TeV Results.” LPCC Special Seminar, Conference Proceedings, 15 Dec 2015.
https://indico.cern.ch/event/442432/contribution/0/attachments/1205563/1756687/CMS_13_TeV_results_public.pdf. Accessed 25 Dec 2015.
- [28] D. Castelvecchi. “Hint of new boson at LHC sparks flood of papers.” *Nature: International Weekly Journal of Science* Published 24 Dec 2015.
<http://www.nature.com/news/hint-of-new-boson-at-lhc-sparks-flood-of-papers-1.19098>
Accessed 25 Dec 2015.
- [29] P. Mattig. “Standard Model at Hadron Colliders: IV Higgs Boson.” *CERN Summer Student Lectures* 24 July 2014.
- [30] T. Shears. “The Particle World: an introduction to particle physics.” *CERN Summer Student Lectures* 1 July 2014.

- [31] J. Boyd. "Raw Data to Physics Results (3/3)." *CERN Summer Student Lectures* 22 July 2014.
- [32] *google images "calorimeter_principle.png"* Accessed 25 Dec 2015.
- [33] Andrew J. Larkoski, Gavin P. Salam, and Jesse Thaler, "Energy Correlation Functions for Jet Substructure." arXiv:1305.0007v3 [hep-ph] 10 Jul 2013.
- [34] The LHCb Collaboration, Ôb-hadron lifetime measurements with exclusive $b \rightarrow J/\psi X$ decays reconstructed in the 2010 data,Ó LHCb-ANA-2011-001.
- [35] ÔPerformance of the ATLAS Secondary Vertex b-tagging Algorithm in 7 TeV Collision Data,Ó Tech. Rep. ATLAS-CONF-2010-042, CERN, Geneva, June 2010.
- [36] ATLAS Collaboration, T. Gopfert, ÔTagging b-jets in ATLAS,Ó Prepared for 24th International Symposium on Lepton-Photon Interactions at High Energy (LP09), Hamburg, Germany, 17-22 Aug 2009.
- [37] Nagai, Yoshikazu. "b-tagging in ATLAS." CPPM Marseille.